

Wavelike Oscillations in High Latitude Thermospheric Doppler Temperature and Line-of-Sight Wind Observed Using All-Sky Imaging Fabry-Perot Spectrometers

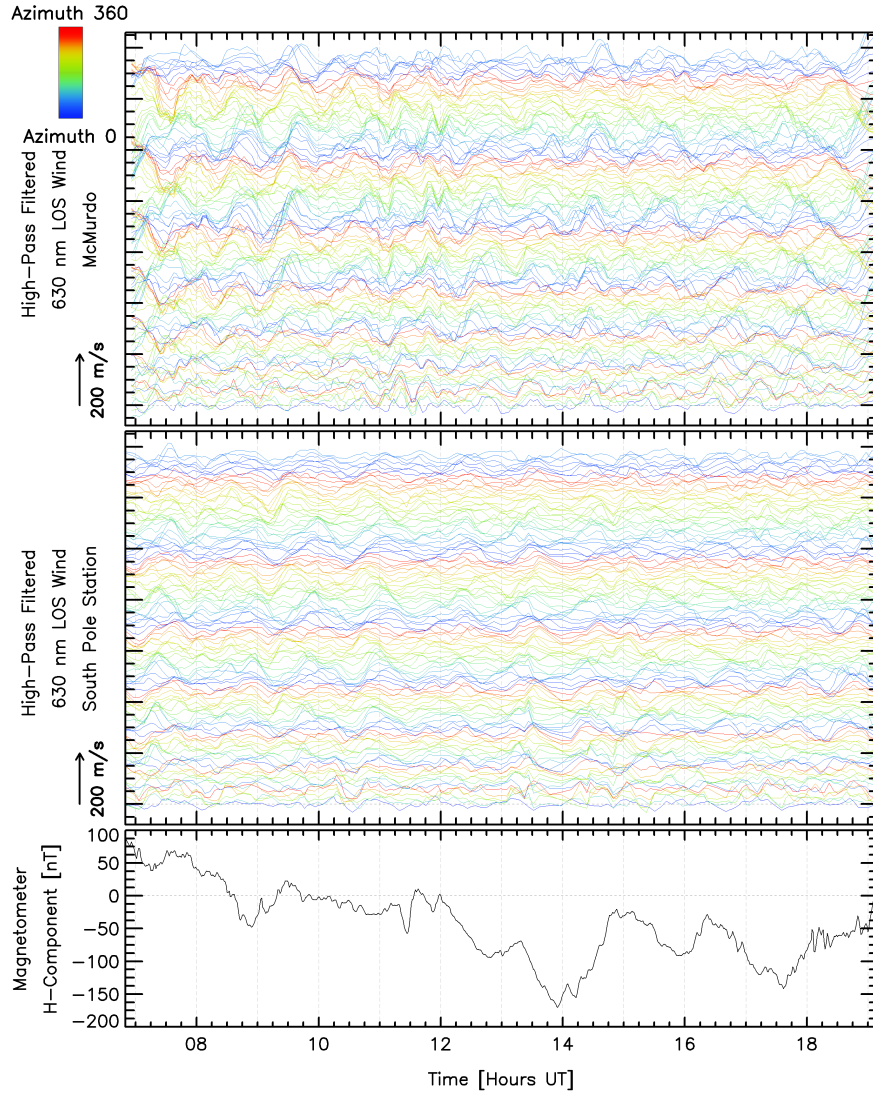
Rajan Itani¹ and Mark G Conde¹

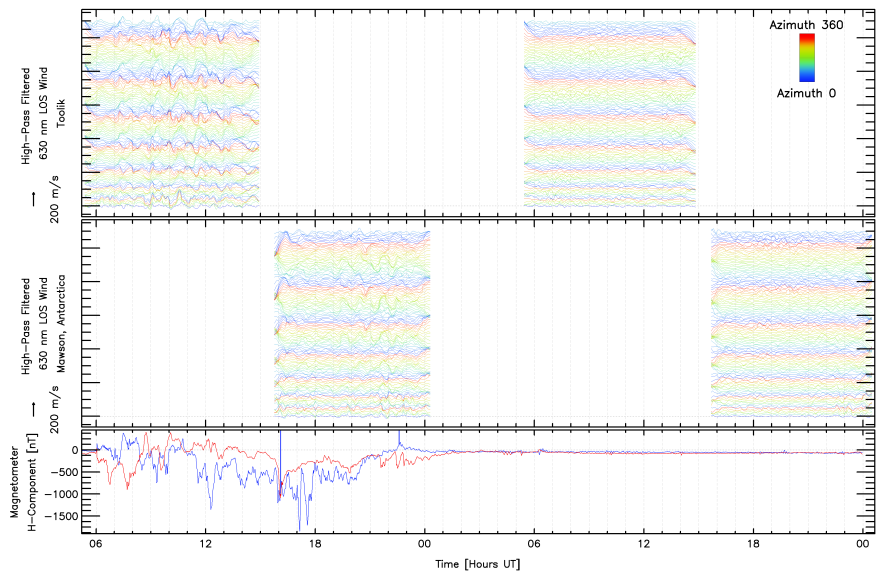
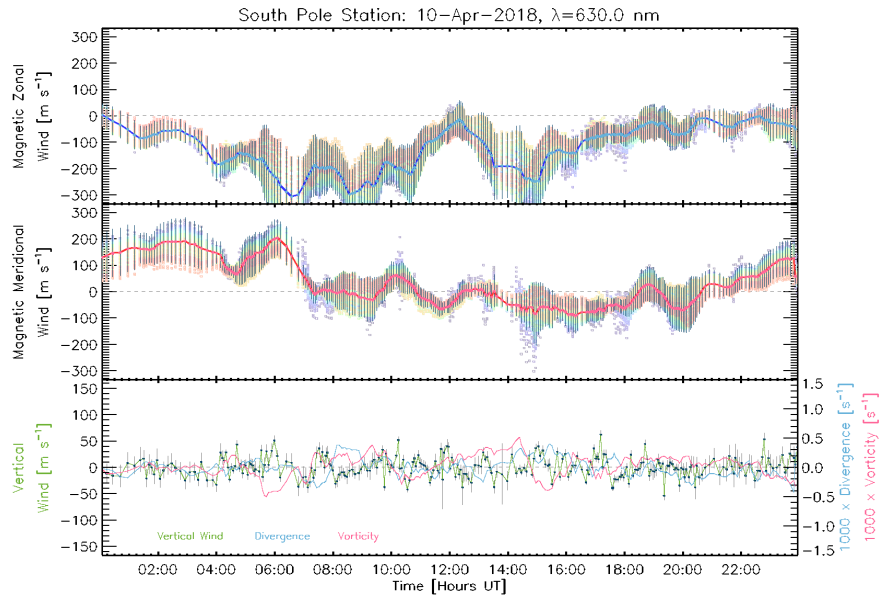
¹University of Alaska Fairbanks

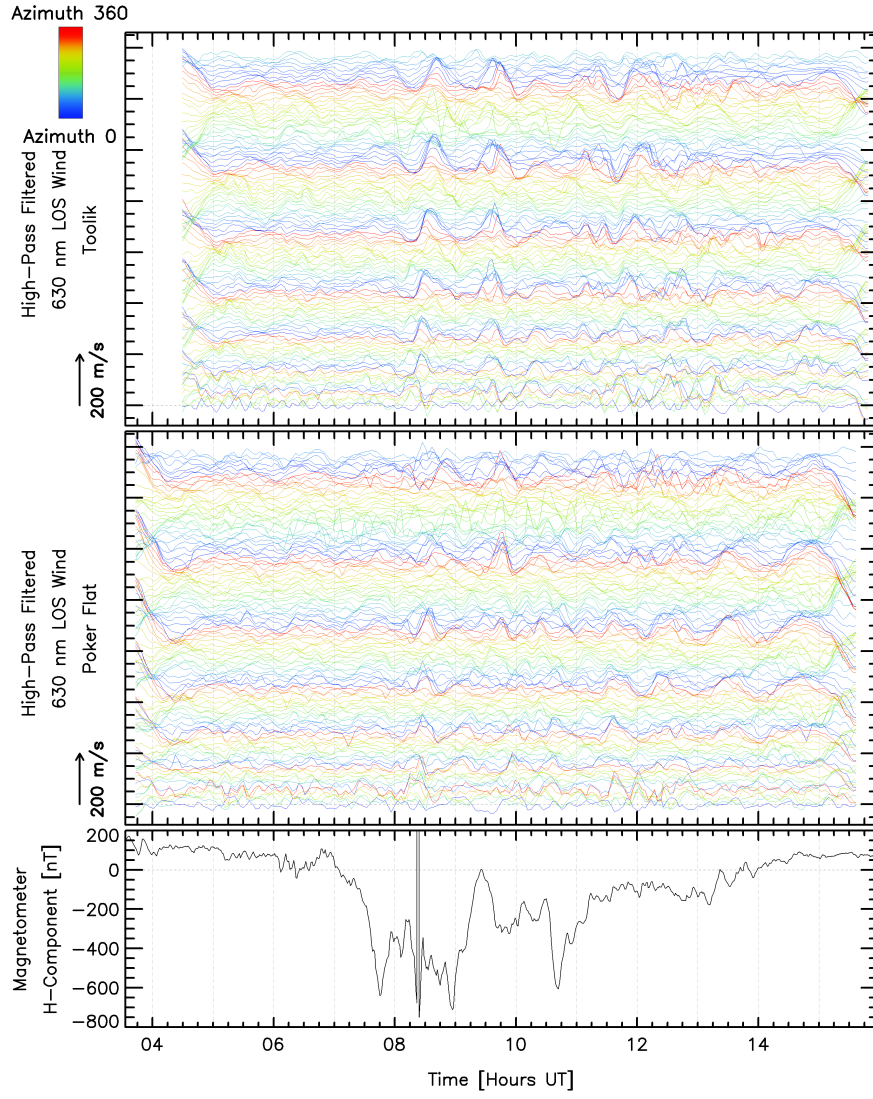
January 20, 2023

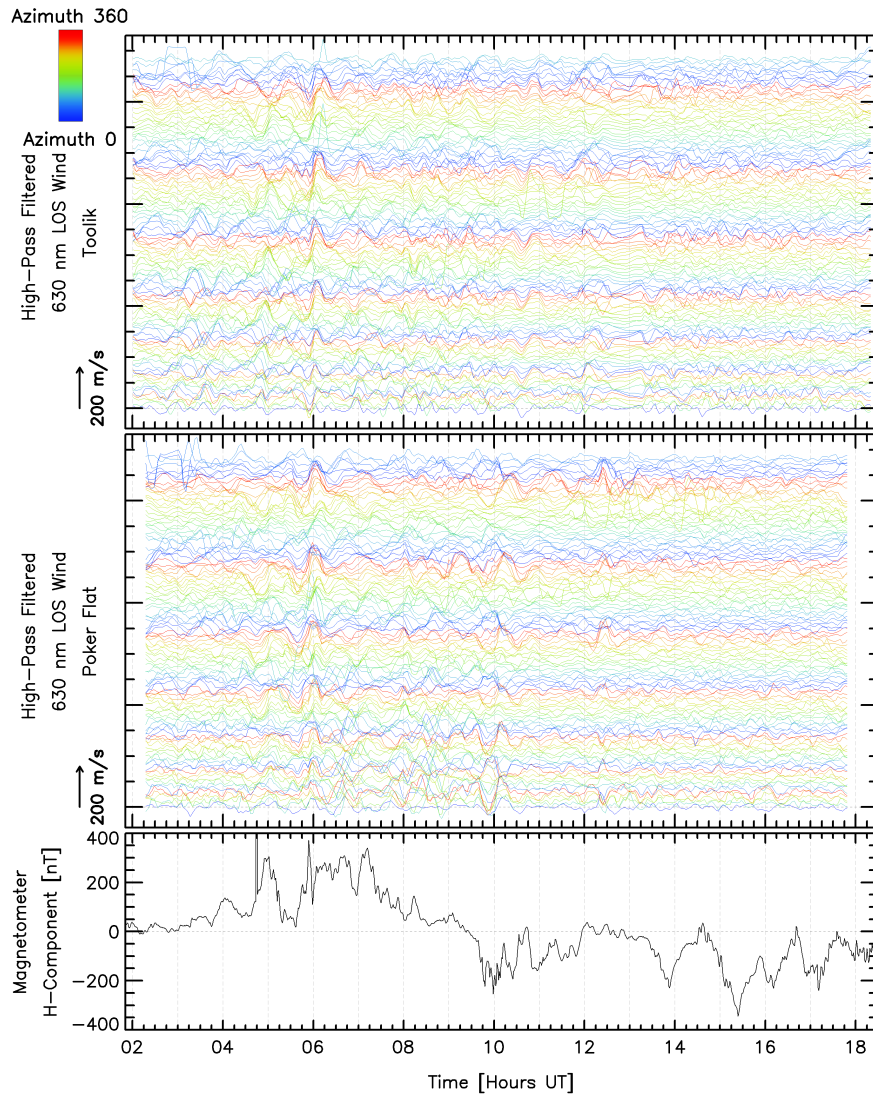
Abstract

Multiple years of thermospheric wind and temperature data were examined to study gravity waves in Earth's thermosphere. Winds and temperatures were measured using all-sky imaging optical Doppler spectrometers deployed at three sites in Alaska, and three in Antarctica. For all sites, oscillatory perturbations were clearly present in high-pass temporally filtered F-region line-of-sight (LOS) winds for the majority of the clear-sky nights. Oscillations were also discernible in E-region LOS wind and F-region Doppler temperature, albeit less frequently. Oscillation amplitudes correlated strongly with auroral and geomagnetic activity. Observed wave signatures also correlated strongly between geographically nearby observing sites. Amplitudes of LOS wind oscillations were usually small when viewed in the zenith and increased approximately with the sine of the zenith angle – as expected if the underlying motion is predominantly horizontal. The SDI instruments observe in many look directions simultaneously. Phase relationships between perturbations observed in different look directions were used to identify time intervals when the oscillations were likely to be due to traveling waves. However, a portion of the instances of observed oscillations had characteristics suggesting geophysical mechanisms other than traveling waves – a recognition that was only possible because of the large number of look directions sampled by these instruments. Lomb-Scargle analysis was used to derive examples of the range of temporal periods associated with the observed LOS wind oscillations. F-region wind oscillations tended to exhibit periods typically ranging from 60 minutes and above. By contrast, E-region wind oscillation periods were as short as 30 minutes.









Abstract

Multiple years of thermospheric wind and temperature data were examined to study gravity waves in Earth's thermosphere. Winds and temperatures were measured using all-sky imaging optical Doppler spectrometers deployed at three sites in Alaska, and three in Antarctica. For all sites, oscillatory perturbations were clearly present in high-pass temporally filtered F-region line-of-sight (LOS) winds for the majority of the clear-sky nights. Oscillations were also discernible in E-region LOS wind and F-region Doppler temperature, albeit less frequently. Oscillation amplitudes correlated strongly with auroral and geomagnetic activity. Observed wave signatures also correlated strongly between geographically nearby observing sites. Amplitudes of LOS wind oscillations were usually small when viewed in the zenith and increased approximately with the sine of the zenith angle – as expected if the underlying motion is predominantly horizontal. The SDI instruments observe in many look directions simultaneously. Phase relationships between perturbations observed in different look directions were used to identify time intervals when the oscillations were likely to be due to traveling waves. However, a portion of the instances of observed oscillations had characteristics suggesting geophysical mechanisms other than traveling waves – a recognition that was only possible because of the large number of look directions sampled by these instruments. Lomb-Scargle analysis was used to derive examples of the range of temporal periods associated with the observed LOS wind oscillations. F-region wind oscillations tended to exhibit periods typically ranging from 60 minutes and above. By contrast, E-region wind oscillation periods were as short as 30 minutes.

Plain Language Summary

Atmospheric neutral wind and temperature measurements from polar regions were analyzed for two different altitudes – ~ 120 km and ~ 240 km. Ripples, also known as atmospheric gravity waves, were a nearly ubiquitous feature of winds observed in our data in the upper altitude region. Oscillations were also detected in upper region temperatures and lower region winds, although these later oscillations were weaker than those of the upper region winds. These oscillations, if visualized, would appear as a complicated wave field manifesting various sizes and propagation directions, in a manner somewhat analogous to surface waves on the ocean. Amplitudes of these oscillations responded strongly to geomagnetic activity, with large waves occurring after the onset of strong mag-

netic perturbations and persisting for several hours. Our instruments sample more than a hundred look directions in the sky at once. This allows for higher confidence in extracting wave signatures than would be possible using data from just a single look direction.

1 Introduction

Earth's thermosphere is convectively stable and has a very high kinematic viscosity, which means that small-scale wind structures are not expected to form in the absence of strong and localized external forcing (e.g., Killeen & Roble, 1988; Killeen et al., 1988). Nevertheless, air parcels displaced vertically by local forcing would experience a restoring force due to an imbalance between buoyancy and gravity. This mechanism would allow so-called gravity waves (GWs) to propagate away from the disturbance. There is ample evidence that such waves are indeed commonly observed in the thermosphere (e.g., Hocke et al., 1996; Oliver et al., 1997; Djuth et al., 1997, 2004; Yigit & Medvedev, 2012; England et al., 2020).

Thermospheric GWs can either be generated in situ or can result from dissipation and breaking of waves propagating upward from lower atmospheric layers (Fritts & Alexander, 2003; Vadas & Fritts, 2006). In-situ generation of GWs in the auroral zone is a common outcome of geomagnetic disturbances (Oyama et al., 2001). GWs generated by mechanisms involving local energy deposition in the thermosphere typically have large relative amplitudes compared to similar waves in the lower atmosphere and have wavelengths larger than 1000 km (Garcia et al., 2016). They are thus relatively easy to observe. Observations show that large-scale thermospheric GWs occur even during quiet geomagnetic conditions suggesting that such waves may have been excited from below (Vadas & Liu, 2009; Bruinsma & Forbes, 2008). All but the largest scale of waves propagating upwards from the lower atmosphere dissipate before reaching the thermosphere. Dissipation of upward propagating waves deposits energy and momentum into the background atmosphere, which generates a broad spectrum of secondary GWs, better suited to survive in the thermosphere (Vadas & Azeem, 2020). These secondary GWs exhibit horizontal scales that are much larger than those of the primary GWs (Vadas et al., 2018).

Itani & Conde (2021) investigated an abrupt stalling of the cross-polar jet in the midnight sector over Alaska. They reported that the characteristic length scale of the stalling could be as short as ~ 200 km. Further, Innis (2000) has reported more gradual

76 stalling of the cross-polar jet. Innis (2000) suggested that one of the possible mechanisms
77 for the stalling of the cross-polar jet could be the dissipation of gravity waves. These ob-
78 servations suggest that gravity waves may play an important role in thermospheric dy-
79 namics. However, details of this role are not fully understood, partly because of the dif-
80 ficulty of observing these waves across an extended geographic region – which is one of
81 the major motivations for the present study.

82 A number of techniques have been used for observing thermospheric gravity waves
83 (England et al., 2020, and references therein). For example, waves cause brightness vari-
84 ations in monochromatic (narrow-band) images of upper atmospheric airglow recorded
85 by all-sky cameras. Low Earth orbit satellites cannot observe temporal evolution at a
86 fixed location because of their orbital motion. Nevertheless, spacecraft can monitor wave
87 perturbations along the orbit at what is essentially an instantaneous time because, at
88 an average orbital speed of ~ 8 km/sec, the time taken to move a distance comparable
89 to the wave’s horizontal wavelength is generally significantly less than the wave’s tem-
90 poral period. However, there is no guarantee that the orbital direction is parallel to the
91 wave’s horizontal k -vector, which means that orbiting spacecraft measure the horizon-
92 tal trace wavelength rather than the intrinsic wavelength. Radio techniques such as ionoson-
93 des, radars, and total electron content measured by GNSS networks can also be used to
94 detect GWs. These methods are sensitive to wave perturbations in ionospheric electron
95 density. Waves observed through electron density fluctuations are typically referred to
96 as traveling ionospheric disturbances.

97 The techniques discussed above provide measurements of a number of different at-
98 mospheric parameters. However, some of these parameters are more directly related to
99 wave propagation than others. Temperature, wind, pressure, and mass density are the
100 fluid fields involved in the dynamical response that allows waves to propagate. The ex-
101 istence and characteristics of GW oscillations can be observed via perturbations in these
102 quantities. Alternatively, other indirect proxy fields may be observed to infer the exis-
103 tence and characteristics of thermospheric GWs. Common examples of wave detection
104 via proxy fields would be through imaging airglow variations (Hickey et al., 2010; Fukushima
105 et al., 2012; Paulino et al., 2016), or recording oscillatory changes in ionospheric elec-
106 tron density (Galvan et al., 2011). The distinction between primary and proxy fields is
107 whether the perturbations are associated with the wave’s restoring force and propaga-
108 tion mechanism. Proxy fields play no role in the wave propagation mechanism.

109 2 Instruments and Methods

110 2.1 Instrumentation

111 An ordinary technique for ground-based remote sensing of thermospheric wind and
112 temperature uses optical Doppler spectroscopy of airglow and/or auroral emissions. In
113 this study, thermospheric winds and temperatures (and oscillatory perturbations to these
114 quantities) were derived from Doppler shifts and Doppler broadening, measured using
115 all-sky imaging Fabry-Perot spectrometer (FPS) instruments. FPSs have been used in
116 several studies that have adopted this technique (e.g., Hays et al., 1969; Hernandez, 1982;
117 Innis et al., 1996; Conde et al., 2001; Nicolls et al., 2012). However, until recently, the
118 sensitivity of typical instruments provided limited ability to characterize the wave os-
119 cillations in the primary fields. The latest generations of FPSs now offer much-improved
120 sensitivity. The particular implementation of the FPS technique used here is known as
121 a Scanning Doppler Imager (SDI), which exploits high sensitivity to provide the capa-
122 bility to look in many directions at once. This makes wave characterization much more
123 tractable than before. Our group has been operating SDIs for more than 20 years. In
124 this work, SDI data have been used to extract periodic perturbations in temperature and
125 line-of-sight (LOS) wind. Further, data were examined from instruments in both the north-
126 ern hemisphere (Alaska) and the southern hemisphere (Antarctica). To our knowledge,
127 this is the first study to compare thermospheric wave activity in both hemispheres us-
128 ing passive optical Doppler spectroscopy.

129 The object-space SDI field of view in the sky can be configured to encompass any
130 solid angle (up to 2π steradian). The typical configuration views a zenith-centered field
131 that extends out to about 75 degrees zenith angle. This field of view is subdivided (us-
132 ing image processing software) into many different contiguous sub-fields arranged in a
133 set of concentric rings divided into sectors. The sub-fields are referred to as “zones”, of
134 which there are 115 in total for the standard configuration. An example of the standard
135 zone map, projected onto an altitude of 240 km, is shown in Figure 1 of Anderson et al.
136 (2012a) for instruments located at Gakona and Poker Flat in Alaska. There are several
137 rings (typically seven) around the zenith, and each of the rings spans 360° in azimuth.
138 There are more azimuthal sectors in the outer rings, so the solid angles subtended by
139 all zones are approximately similar.

140 Exposure times typically vary in the range of two minutes to ten minutes. Within
 141 any given exposure the SDI records the optical spectrum of the airglow/aurora for each
 142 zone, over a wavelength interval spanning approximately 10 nm, with a spectral reso-
 143 lution of 1 nm or less. The sky spectrum is then fitted numerically to derive the Doppler
 144 temperature and LOS component of the wind associated with each zone. An example
 145 of the resulting data acquired by an SDI observing in its standard mode is depicted in
 146 Figure 1 of Conde et al. (2018).

147 For the present work, SDI data were examined from three Alaskan sites (Toolik Lake,
 148 Poker Flat, and Gakona) and three Antarctic sites (Mawson, McMurdo, and the South
 149 Pole). The geographic locations of these six sites are given in Table 1. SDIs provide use-
 150 ful diagnostics for studying thermospheric gravity waves because they measure the tem-
 151 perature and wind fields that are directly associated with the wave propagation in the
 152 thermosphere (i.e. they are not proxy fields). Furthermore, the all-sky imaging capabil-
 153 ity allows the construction of 2D-geographic maps of the perturbation fields.

Table 1. Geographic locations of the six different SDI instruments deployed in Alaska and Antarctica used in this work. Coordinates have been rounded to the nearest arc minute.

Station Name	Latitude	Longitude
Toolik Lake	68° 38' N	149° 36' W
Poker Flat	65° 7' N	147° 29' W
Gakona (HAARP)	62° 24' N	145° 9' W
Mawson	67° 36' S	62° 52' E
McMurdo	77° 50' S	166° 40' E
South Pole	90° 0' S	--

154 SDI instruments operate automatically and observe the sky whenever the solar de-
 155 pression angle exceeds 9 degrees (which is required to allow the weak airglow or auro-
 156 ral emissions to be isolated from the background scattered sunlight). Unfortunately, the
 157 resulting data do contain periods when the measurements are not indicative of geophys-
 158 ical conditions in the thermosphere – for example due to observing through the heavy
 159 tropospheric cloud or as a result of serious instrumental problems. For this study, many
 160 nights of automatically acquired data were examined. The first step in data processing

161 was to apply various quality parameters to select only those periods when the measure-
162 ments satisfied well-established criteria for validity.

163 2.2 The Routine Vector Wind Product

164 The standard analysis of SDI spectra that satisfy the criteria for validity produces
165 115 estimates of the LOS component of the wind observed in each look direction. Sub-
166 sequent analysis is then used to estimate zonal and meridional wind components for each
167 zone at each time. Figure 1 shows examples of the time series of the medians of the fit-
168 ted vector wind components over all 115 look directions, observed from Earth's geographic
169 South Pole on the night of April 10, 2018. The winds are resolved into magnetic zonal
170 and meridional components using a Cartesian coordinate system in which the magnetic
171 north direction is defined by the oval angle specified by the VITMO magnetic field model
172 (<https://omniweb.gsfc.nasa.gov/vitmo/cgm.html>). Vertical bars in the top and mid-
173 dle panels of Figure 1 do not indicate wind uncertainties. Rather, they indicate the stan-
174 dard deviation of values observed in the wind components across all the zones at each
175 time. A larger vertical bar indicates greater wind variation across the field of view.

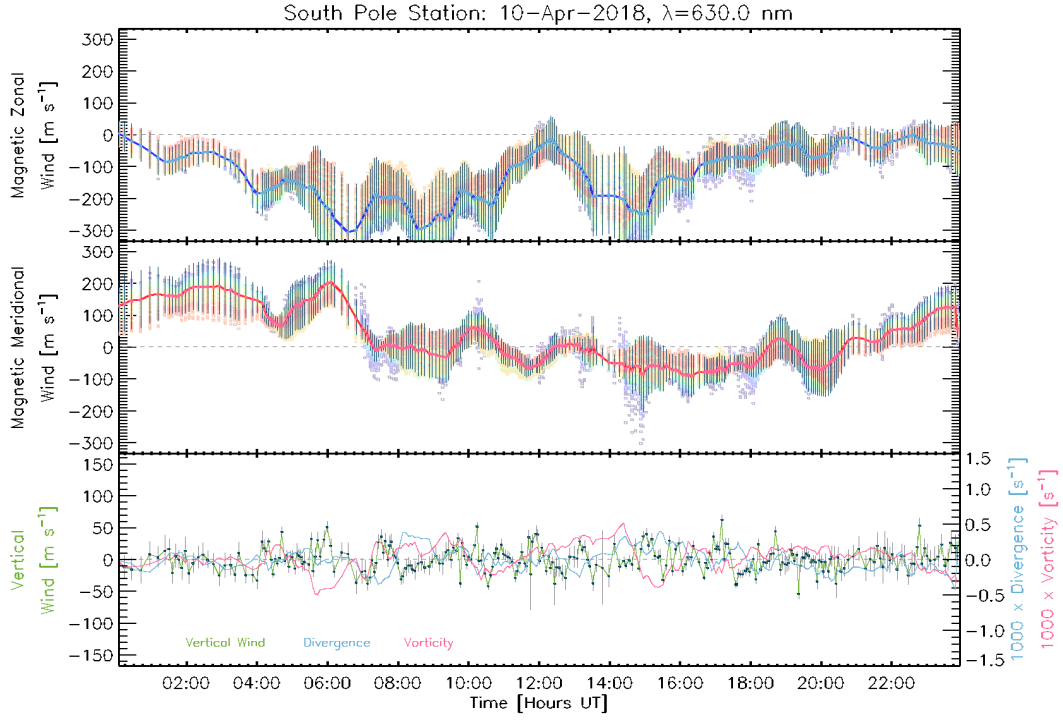


Figure 1. Wind summary plot derived from 630 nm spectra (originating from F-region heights) for the day of April 10, 2018, as observed from the Earth’s geographic South Pole. The solid blue and red traces in the top and middle panels respectively show the median of the fitted magnetic zonal and magnetic meridional winds from all look directions at a given time. Individual dots in these panels are color-coded according to the look azimuths and represent the fitted wind in each zone. The rainbow-colored swaths around the traces are composed of a number of those dots, most of which are unresolved. A few of them are discernible away from the curves. Black vertical bars on top of the median wind traces show the standard deviation of observed wind speeds in all the zones at a given time. The bottom panel shows vertical wind, horizontal divergence, and horizontal vorticity as indicated by the color of the traces. Note that geographic zonal and meridional directions are undefined at the pole. However, no such problem applies to the geomagnetic directions used here.

176 Although the fitted vector wind components are of most interest for understand-
 177 ing thermospheric dynamics at synoptic scales and larger, the fitting process generates
 178 vector components using all 115 zones together. Further, it requires several substantial
 179 assumptions (Conde & Smith, 1998; Anderson et al., 2012b). However, the horizontal
 180 wavelengths of thermospheric gravity waves are comparable to or smaller than the syn-

181 optic scale. A product derived from all look directions across the ~ 1000 km diameter
 182 field of view would suppress fluctuations that are local to one (or just a few) of the look
 183 directions. Further, the required assumptions, while reasonable when applied over the
 184 whole field of view, are almost certainly inappropriate for single-zone data. Overall, the
 185 fitted vector winds most likely would not capture wave oscillations very accurately. There-
 186 fore, for extraction of wave perturbations, it is far better to use the original LOS wind
 187 estimates, which are derived solely from the spectra observed in individual zones.

188 **2.3 Signal Processing: Extraction of Perturbations in Temperature and** 189 **LOS Wind**

190 A high-pass temporal filter was used to extract high-frequency oscillations in the
 191 observed temperatures and LOS winds. Wind and temperature perturbations were ob-
 192 tained, for each zone, as a function of time during the night. The filter transmission was
 193 tuned to begin attenuating periods longer than ~ 180 minutes. Variations over time scales
 194 longer than this are likely to reflect the slowly varying forcing experienced by the ther-
 195 mosphere as a result of changing local time, and hence may not be indicative of trav-
 196 eling waves. Additionally, oscillation periods of five minutes or less were suppressed in
 197 the current analysis to attenuate noise. Such filtering is unlikely to conceal any valid geo-
 198 physical information because 5 minutes is less than the Brunt-Väisälä period at F-region
 199 altitudes and less than or comparable to it in E-region (Yeh & Liu, 1974; Yu, 2007). Fi-
 200 nally, the sampling cadence of SDI data is typically longer than five minutes except un-
 201 der active geomagnetic conditions.

202 Figure 2 presents an example of the result of applying the high-pass filter to the
 203 115 time series of LOS winds. In this format (which is also used for a number of sub-
 204 sequent figures) high-pass filtered signals from each zone are plotted with a small ver-
 205 tical displacement between successive traces to produce a stack plot. The ordering of traces
 206 in the stack is such that the traces near the bottom correspond to zones near the zenith,
 207 whereas those near the top represent zones near the horizon. The color of the traces in
 208 the wave plots indicates the viewing azimuth relative to the magnetic north, according
 209 to the color scale bar. The sector immediately east of zero degrees magnetic azimuth is
 210 depicted with the blue hue seen at the bottom of the color scale bar. As azimuth increases,
 211 hues from progressively higher levels in the scale bar are used until the red color, which
 212 corresponds to the sector immediately west of zero degrees azimuth. Because there are

213 more azimuthal sectors near the horizon than near the center, the color banding is more
 214 spread near the top of the wave plots.

215 Many days of SDI data from various stations have been examined in this study. Wave-
 216 like oscillatory wind and temperature perturbations appeared very commonly during clear-
 217 sky observations. To illustrate the types of behavior observed, six days of data that ex-
 218 hibited pronounced oscillatory perturbations have been chosen from the observational
 219 archive. (As SDI instruments acquire data only during darkness, the word “day” should
 220 only be interpreted as referring to the date of observations.) Lomb-Scargle analysis was
 221 performed to find the typical periods associated with these waves.

222 As will be discussed in later sections, not all oscillatory perturbations seen in the
 223 data are indicative of propagating waves. The best way to unambiguously identify sig-
 224 natures of a propagating wave would be to reconstruct the phase fronts and the prop-
 225 agation directions based on phase lags between the various look directions. However, such
 226 analysis is not straightforward and is beyond the scope of this initial survey. Rather, this
 227 preliminary study will instead merely flag examples in which perturbations across a large
 228 portion of the field of view manifest phase lags that appear qualitatively consistent with
 229 a propagating wave, and determine whether such events appear to be correlated with
 230 times of elevated geomagnetic activity.

231 **3 Results**

232 Oscillatory perturbations were observed in LOS winds during most (if not all) of
 233 the data that passed the quality controls. In many cases, the oscillations were weak but
 234 unambiguously present. Strong oscillatory perturbations typically corresponded to times
 235 of elevated magnetic activity. These general behaviors are illustrated by the following
 236 examples.

237 **3.1 Wavelike Perturbations in Doppler Temperatures and LOS Wind** 238 **Components**

239 ***3.1.1 F-Region LOS Wind Oscillations***

240 The top and middle panels in Figure 2 show wavelike oscillations in LOS winds recorded
 241 by SDI instruments located at McMurdo and the South Pole stations in Antarctica, dur-
 242 ing the same night as shown in Figure 1 – i.e., April 10, 2018. These wind oscillations

243 were extracted from the LOS components of winds derived from 630.0 nm atomic oxy-
 244 gen spectra. The bottom panel shows the geomagnetic H-component recorded during
 245 this period at Scott Base, Antarctica, which is ~ 3 km from McMurdo Station. Wave ac-
 246 tivity was moderately disturbed on this day relative to the activity levels seen on many
 247 of the days in our archive. Consistent with other examples presented here, this level of
 248 wave activity was commensurate with the moderately disturbed magnetic activity on this
 249 day as indicated by the lower panel of Figure 2 and three hourly Kp indices for the ob-
 250 servation period which were 4, 3-, 3+, 3, and 2+. The solar radio flux index (F10.7) was
 251 68.8 solar flux unit (sfu), although there does not appear to be a strong correlation be-
 252 tween F10.7 and wave activity within the archived observations. Note that Figure 1 shows
 253 a large-scale background wind. This has been removed from all the stack plots presented
 254 in this paper by the high-pass filtering process.

255 McMurdo and South Pole instruments are independent, and these stations are ge-
 256 ographically separated by a large distance (~ 1350 km), which means that their F-region
 257 fields of view do not overlap. Nevertheless, there is some indication that the most ac-
 258 tive period in the South Pole data also corresponded to energetic wave activity at Mc-
 259 Murdo. The amplitudes of perturbations in Figure 2 (and in subsequent LOS wind stack
 260 plots) are smallest for zones near the zenith and they increase gradually toward the outer
 261 zones closer to the horizon, as would be expected if the oscillations were primarily due
 262 to perturbations in the horizontal wind. These characteristics strongly indicate an ac-
 263 tual geophysical origin for the wave oscillations extracted from the observations. Note
 264 that the oscillations are not simple sinusoids, illustrating that the perturbations are not
 265 monochromatic.

266 Importantly, the data frequently showed phase progressions among the look azimuths.
 267 Phase shifts among the oscillations arising from different parts of the sky are conspic-
 268 uous in the lower panel of Figure 2 at ~ 14 UT. Another example of phase evolution in
 269 the LOS components of the wind can also be seen between 9-10 UT in the upper panel
 270 in Figure 2. In this figure, looking at the oscillations coming from similar azimuths (traces
 271 in the same color), the peak oscillations shift by ~ 15 minutes for the traces near the top
 272 of the plot relative to the traces near the bottom. This behavior is as expected consid-
 273 ering the previously observed propagation speeds (~ 500 m/s) of storm time F-region wind
 274 oscillations (Johnson et al., 1995), and the ~ 500 km radius of all-sky field of view of the
 275 SDI instrument at 240 km altitude.

276 On this night, oscillation amplitudes recorded at McMurdo were larger than that
277 at the South Pole. Caution should be taken that the high-pass filtered wind perturba-
278 tion amplitude varies not only because of multiple look elevation angles in the field of
279 view but also due to the projection effect of various LOS wind components onto the vary-
280 ing azimuth angles of the look directions. It is quite difficult to fully resolve the contri-
281 butions of these two effects for data presented in the stack plot format.

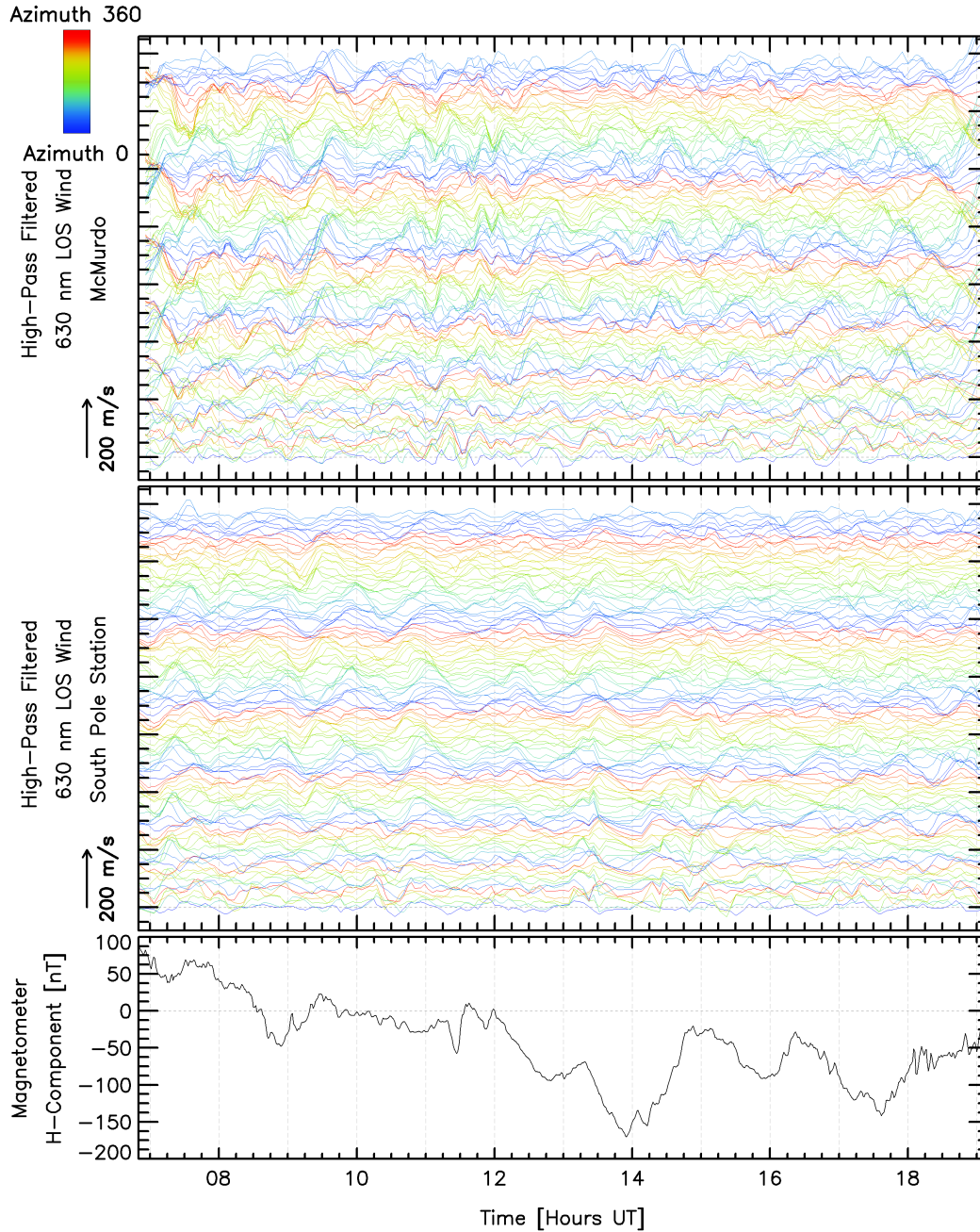


Figure 2. The top and middle panels show LOS wind oscillations observed from McMurdo and South Pole stations respectively, during the night of April 10, 2018. The magnitude of LOS wind oscillations is indicated by the scale arrow on the bottom left of each panel. The color bar on the top left shows the azimuthal directions of the zones to which the stacked wave plots correspond. Traces near the bottom of each of the top two panels correspond to zones near the zenith, whereas those toward the top represent zones near the horizon. Each field of view was divided into 115 zones, and hence there are 115 independent traces in each panel. The bottom panel shows the trace of the magnetometer H-component observed at Scott Base, Antarctica.

282 **3.1.2 Simultaneous Oscillation Signatures in LOS Wind Data Captured**
 283 **by Nearby SDIs**

284 There were many instances where SDI instruments with some overlap in their field
 285 of view simultaneously observed similar oscillatory features in their high-pass filtered LOS
 286 wind data. For example, the top and middle panels in Figure 3 respectively show wave-
 287 like perturbations in F-region LOS winds as observed from Toolik Lake and Poker Flat,
 288 Alaska on October 14, 2016. The bottom panel shows the H-component of the geomag-
 289 netic field perturbation, recorded at College, Alaska, which is ~ 30 km southwest of Poker
 290 Flat. The two SDI observing sites are located ~ 400 km apart and have some overlap (more
 291 than 60 %) in their fields of view at ~ 240 km altitude. The collection and analysis of
 292 data from these two instruments are completely independent; there is no instrumental
 293 or data processing mechanism that could couple the results shown in the top two pan-
 294 els of Figure 3. Nevertheless, the time series of high-pass filtered LOS wind from each
 295 station show instances of very similar responses at times, which can only have occurred
 296 as a result of two instruments observing the same geophysical oscillations. In particu-
 297 lar, the onset of a similar burst of oscillations was observed at both sites at ~ 8 UT. Rel-
 298 atively weak wind perturbations prevailed prior to this point. However, after this time,
 299 strong wavelike oscillations persisted for the rest of the night. Note that the dynamic
 300 wave activity began within an hour of the onset of geomagnetic storm conditions. Such
 301 behavior is not unexpected. There were several occurrences in which the responses were
 302 time-synchronous across the fields of view of these two instruments. Such an instance
 303 is discernible at $\sim 8:30$ UT, at both locations, as indicated by large-amplitude responses
 304 occurring almost simultaneously across both fields of view. Such events are almost cer-
 305 tainly not indicative of propagating waves, because a field of moving wave fronts would
 306 result in responses shifted in phase between geographically separated locations. As in
 307 Figure 2, data from these sites also show a gradual increase in perturbation amplitudes
 308 from the zenith toward the horizon indicating the perturbations were associated predom-
 309 inantly with the horizontal wind.

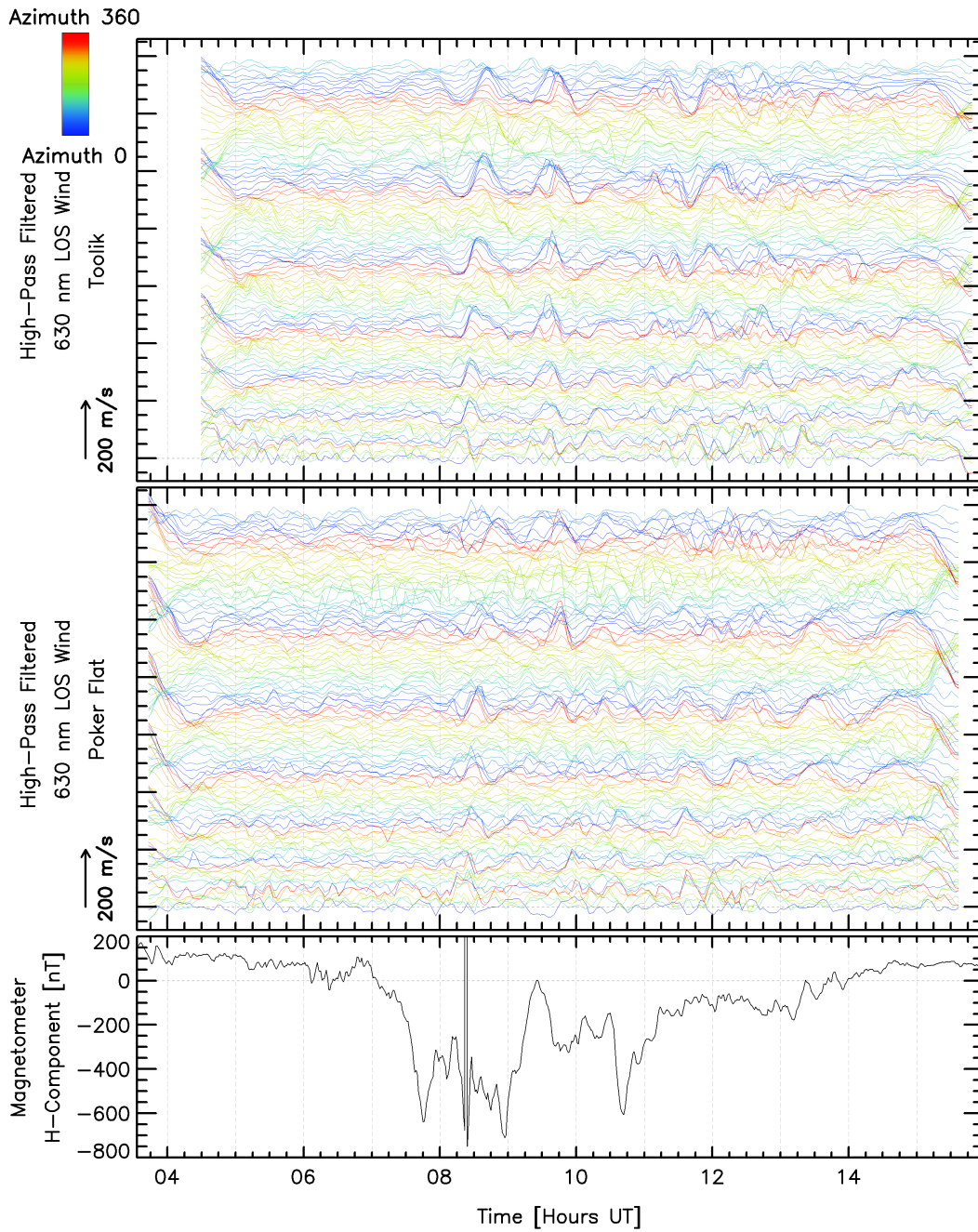


Figure 3. Same as Figure 2, but now showing measurements from Toolik Lake and Poker Flat, Alaska, for the night of October 14, 2016. The bottom panel depicts the H-component of the magnetic field perturbation recorded at College, Alaska. On this day, the F10.7 index was 92.3 sfu, and three hourly Kp indices from 3 UT to 15 UT, which also span the observation period, were 5-, 5-, 3, and 2-.

310 Figure 4 shows an even more dramatic example of two stations simultaneously ob-
311 serving remarkably similar wind perturbations. These data were recorded on January
312 21, 2016, again from Poker Flat and Toolik Lake. The bottom panel shows the magne-
313 tometer trace from College, Alaska, and indicates that this day was geomagnetically ac-
314 tive. Energetic wave activity was seen in the red-line LOS wind oscillations at both lo-
315 cations. A qualitative examination of the time series on this night (and on other nights)
316 suggests a strong tie between the wave oscillation amplitudes and the level of geomag-
317 netic disturbance. As before, the two SDI instruments contributing to Figure 4 operate
318 completely independently of each other. Wavelike perturbations that appear just before
319 the onset of the time-synchronous event at ~ 6 UT provide an example of similar wave
320 signatures observed from two locations. Similar responses between two nearby sites are
321 observed commonly but not ubiquitously. Instances of similar perturbations seen from
322 the two sites occurred throughout the night. The LOS wind perturbations were partic-
323 ularly highly correlated between 12 UT and 13 UT. Nevertheless, the instances of sim-
324 ilar perturbations were superimposed on observations that were clearly independent be-
325 tween the two stations.

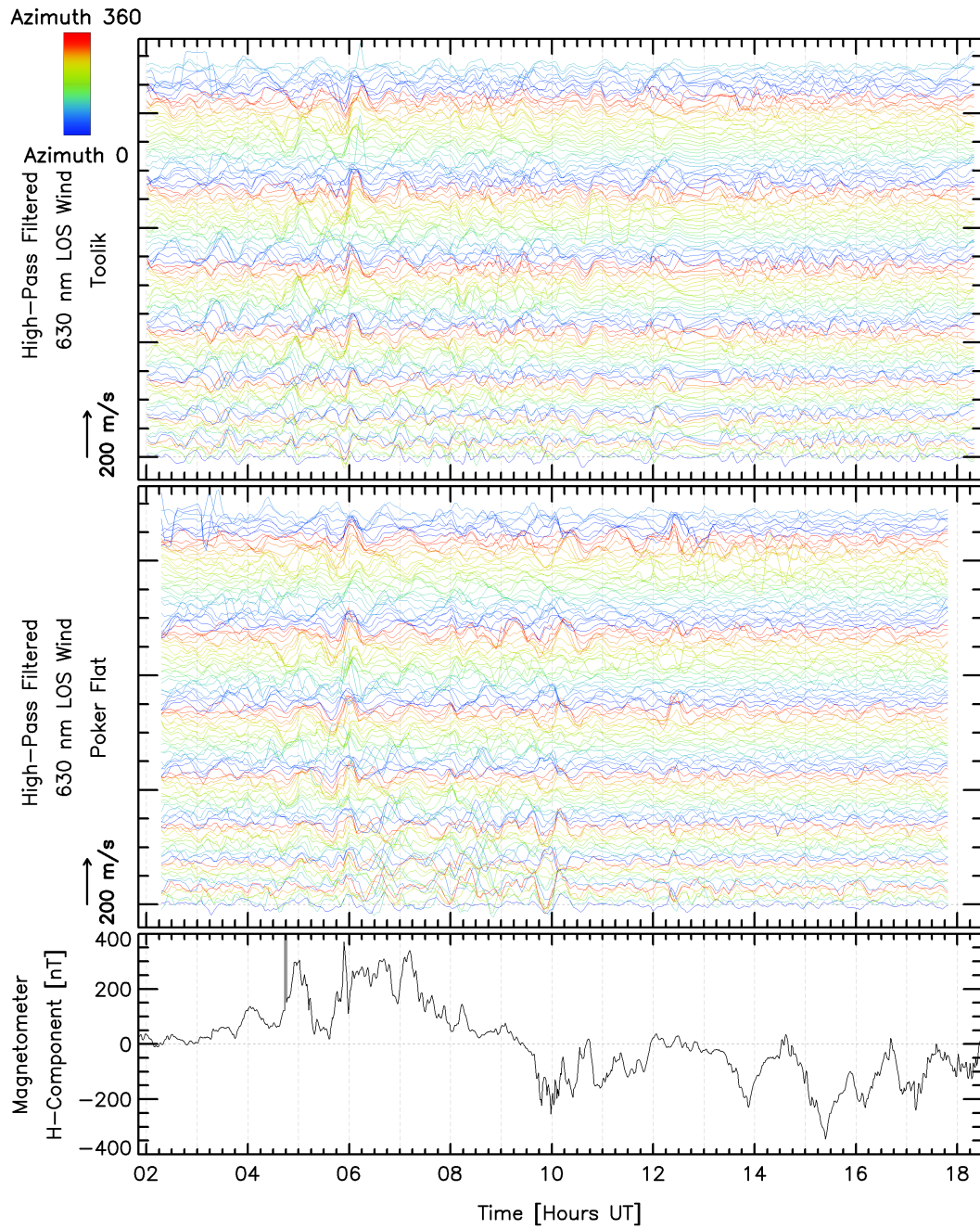


Figure 4. Same as Figure 2 but for the night of January 21, 2016, as observed from Toolik Lake and Poker Flat, Alaska. The bottom panel shows the magnetometer trace from College, Alaska. On this day, the F10.7 index was 100.7 sfu, and three hourly Kp indices for the observation period (2 UT to 18 UT) were 4-, 6-, 5+, 3+, 3-, and 4-.

3.1.3 Hemispheric Comparison of Wave Activity

For hemispheric comparison of wave activity, a two-day period was chosen for which observations were available from Mawson, Antarctica, and Toolik Lake, Alaska. Geomagnetic conditions varied considerably during this period. These two locations lie on broadly similar geographic and geomagnetic latitudes. Because of their high latitude locations, days on which both sites can observe continuously for multiple hours only occur around the equinox. Further, local time at these two sites differs by 14 hours, which means that lengthy periods of truly coincident observations do not occur because SDIs are only capable of recording sky spectra during darkness. Nevertheless, both sites made observations during the extended period shown in Figure 5. Even though the observations did not overlap in time, we can compare whether the two hemispheres responded similarly to magnetic activity.

On March 17, 2013, exceptionally high amplitude wave oscillations were observed from Toolik Lake, Alaska, and Mawson, Antarctica as a result of highly disturbed geomagnetic activity. Note that these oscillations were plotted using a less sensitive scale than other similar figures in this paper because of the large oscillation amplitudes. These were ~ 100 m/s, whereas more typical observed amplitudes were usually ~ 50 m/s or less – except, of course, during very active periods. However, on the following day, the geomagnetic disturbance declined at both sites, as did the wave activity. This result suggests that wavelike perturbation amplitudes co-vary in opposite hemispheres. However, testing for actual conjugacy would require observatories in opposite hemispheres that are located on similar longitudes to allow for observations that are truly coincident in time.

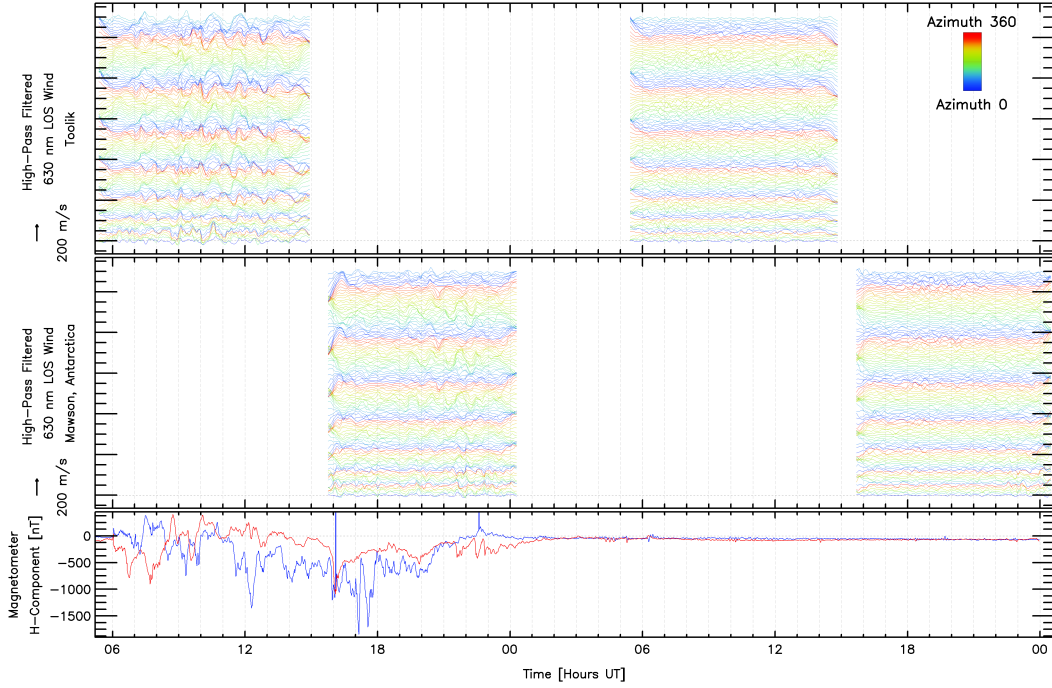


Figure 5. Same as Figure 2 but the upper two panels are showing two days of LOS wind data (March 17 to 18, 2013) from Toolik Lake, Alaska, and Mawson, Antarctica. The bottom panel shows the geomagnetic H-component recorded by the magnetometer located at College, Alaska (blue) and Mawson, Antarctica (red), as indicated by the color of the traces. The spikes in the magnetometer trace from College, Alaska near 16 UT and between 22-23 UT on March 17, 2013, are most likely due to some interference. On March 17, 2013, the F10.7 index was 124.5 sfu, and three hourly Kp indices were 2+, 7-, 6+, 6-, 6+, 7-, and 6. During the observations on March 18, 2013, the three hourly Kp indices were 3, 2+, 2, 2-, 1+, 1-, 2-, and 1+, and the F10.7 index was 116.6 sfu.

348 **3.1.4 Wave Activity Derived from 558 nm Spectra**

349 Figure 6 shows LOS wind oscillations derived from observations from McMurdo Sta-
 350 tion of both the thermospheric 630 nm red-line emission from the F-region, and the 558
 351 nm green-line emission from the E-region. Strong F-region oscillations were observed through-
 352 out the night of April 10, 2018. By contrast, the E-region was mostly placid apart from
 353 a sudden packet of oscillations observed beginning at ~10:00 UT, as seen in the middle
 354 panel of Figure 6. Geomagnetic activity was disturbed throughout much of this night.
 355 The E-region wave event shown in the middle panel, however, occurred while the mag-

356 netometer at Scott Base observed the weakest activity over that whole night. That is,
 357 the magnetometer H -component perturbation trace was flatter and was closer to zero
 358 than at other times during the observation. Despite this, winds in the E-region mani-
 359 fested the largest amplitude oscillations of any time during the night.

360 As shown in Figure 7, the 558 nm auroral emission at ~ 10 -12 UT was associated
 361 with elevated and spatially variable Doppler temperatures. This implies that the emis-
 362 sion was coming from generally higher in the E-region, but with considerable height vari-
 363 ation across the field of view. Since it is known that strong vertical gradients in horizon-
 364 tal winds occur throughout the E-region (Larsen, 2002), the variability in observation
 365 altitude would be expected to be associated with perturbations in measured winds. This
 366 effect is likely to have contributed to the burst of oscillations seen after 10 UT. A com-
 367 parison of the temperature and intensity sky maps (Figures 7 and 8 respectively) shows
 368 that the bright regions corresponded to low-energy auroral precipitation. (This is because
 369 green-line emissions in higher altitudes, corresponding to higher thermospheric temper-
 370 ature, are typically associated with a lower characteristic energy of electron precipita-
 371 tion (Hecht et al., 2006; Kaeppler et al., 2015).) Because of the elevated brightness, it
 372 seems likely that this low-energy precipitation would have carried significant energy flux
 373 (Gabrielse et al., 2021). This energy would have been deposited higher in the E-region
 374 than was the case for most other periods on this night. The heat capacity per unit vol-
 375 ume at these higher altitudes is less (due to reduced mass density) than it would have
 376 been for the altitudes to which electron precipitation penetrated during other times of
 377 this night. The reduced heat capacity may have allowed the soft particle heating to ex-
 378 cite pressure gradients and consequently winds, without requiring electric current, Joule
 379 heating, or any associated geomagnetic disturbance. These overall expectations are con-
 380 sistent with the behavior observed. A final contributor to the burst of LOS wind oscil-
 381 lation seen after 10 UT could be the rapidly varying auroral brightness over time, which
 382 can sometimes introduce artifacts into Doppler spectra derived from the SDI technique.
 383 This mechanism is mostly discussed here for completeness. In this particular case, it is
 384 unlikely to be the major source of the observed E-region perturbations. This is because
 385 amplitudes of the observed perturbations were the smallest for zones near the zenith, whereas
 386 the zenith zones are the ones most sensitive to spectral artifacts of this type. Care should
 387 be taken that these three effects (height variations, particle heating, and spectral arti-
 388 facts) may have accounted for a significant proportion of the observed LOS wind oscil-

389 lations after 10 UT. The current data do not allow us to determine the relative contri-
390 butions from these effects versus perturbations caused by atmospheric wave activity.

391 Although the magnetometer H-component was never highly disturbed, there was
392 at least modest geomagnetic activity for the whole night. (Relevant Kp values are in-
393 cluded in the caption for Figure 6.) Unlike the E-region, waves in the F-region occurred
394 with large amplitudes (~ 100 m/s) for the whole night. The Scott Base magnetometer
395 data, presented in the bottom panel in Figure 6, showed that the geomagnetic activity
396 was more dynamic earlier in the night before SDI observations began. Presumably, the
397 large amplitude F-region waves were triggered by this earlier activity. Alternatively, these
398 red-line wind oscillations, with longer wave periods, dissipate slowly and thus could have
399 propagated to the observation location from a different source region (Yiğit & Medvedev,
400 2019). Oscillation amplitudes increased conspicuously from the zenith toward the hori-
401 zon for both E-region and F-region perturbations. This zenith angle dependence indi-
402 cates that the wind perturbations were primarily associated with horizontal winds.

403 It was initially expected that we would encounter instances of oscillations present
404 at F-region heights as a result of waves propagating up from the lower atmosphere. In
405 this study, the only way to identify potential wave activity driven from below would be
406 to encounter significant wave oscillations during magnetically quiet times. Although wave
407 activity is often present, even at quiet times, it is not possible to determine with any cer-
408 tainty whether small amplitude waves arose as a result of forcing from below, as opposed
409 to being due to in-situ forcing. Of course observation of a large-amplitude wave packet
410 during very quiet geomagnetic conditions would more strongly suggest that these waves
411 were excited from below. However, no clear instances of large amplitude waves during
412 geomagnetically quiet times were found in the data examined for this study. Overall, it
413 is not possible from these data to unambiguously identify instances of forcing from be-
414 low. Nevertheless, clear examples may occur after more extensive observations. Further,
415 we may well have observed waves excited from below but have been unable to establish
416 their origin definitively.

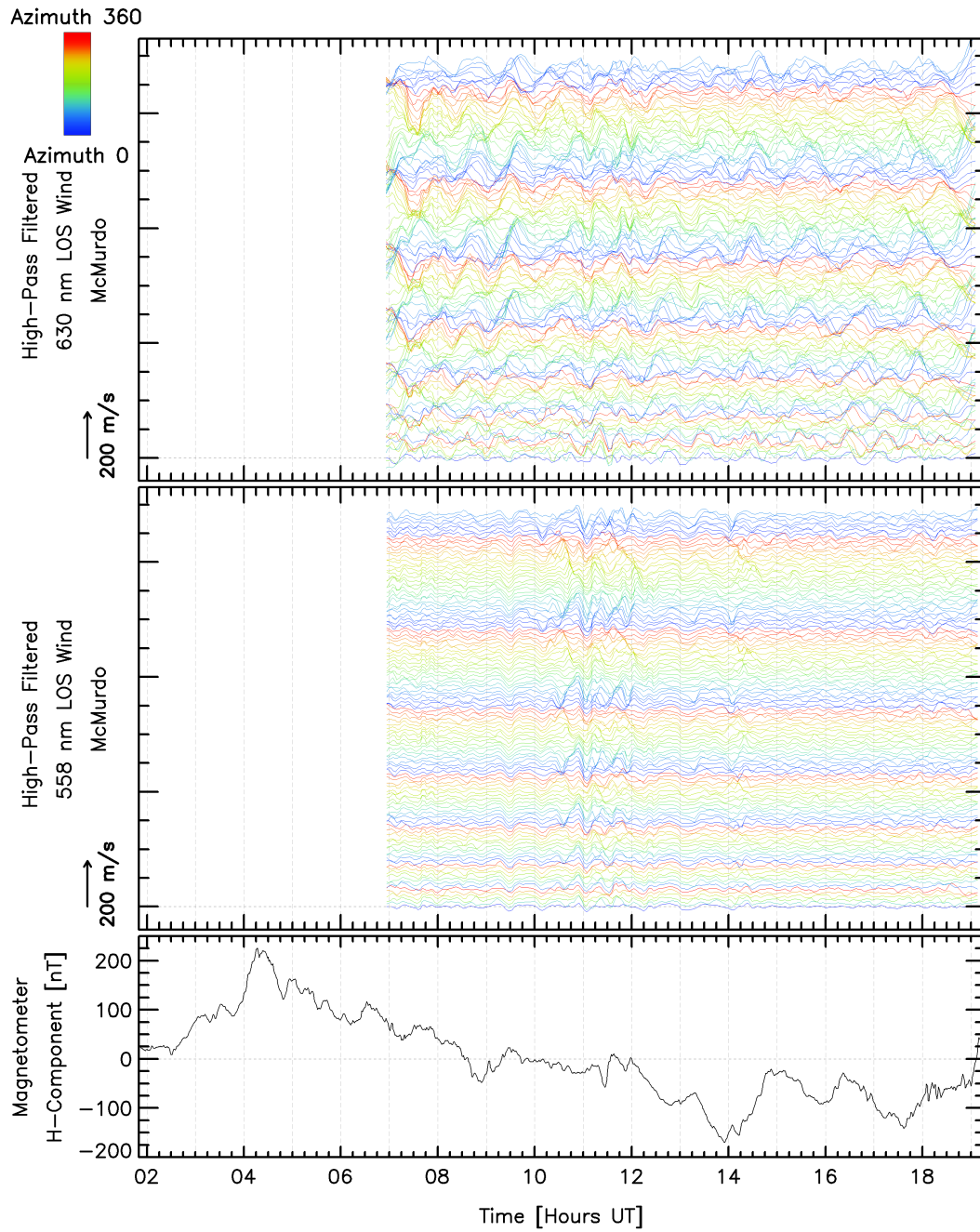


Figure 6. Same as Figure 2 but with top and middle panels respectively showing wave stack plots for F-region and E-region LOS wind perturbations observed from McMurdo Station, Antarctica on April 10, 2018. The bottom panel shows the corresponding fluctuations in the magnetic H-component recorded at Scott Base, Antarctica. On this day, the F10.7 index was 68.8 sfu, and three hourly Kp indices during the data period (6-19 UT) were 4, 3-, 3+, 3, and 2+ respectively.

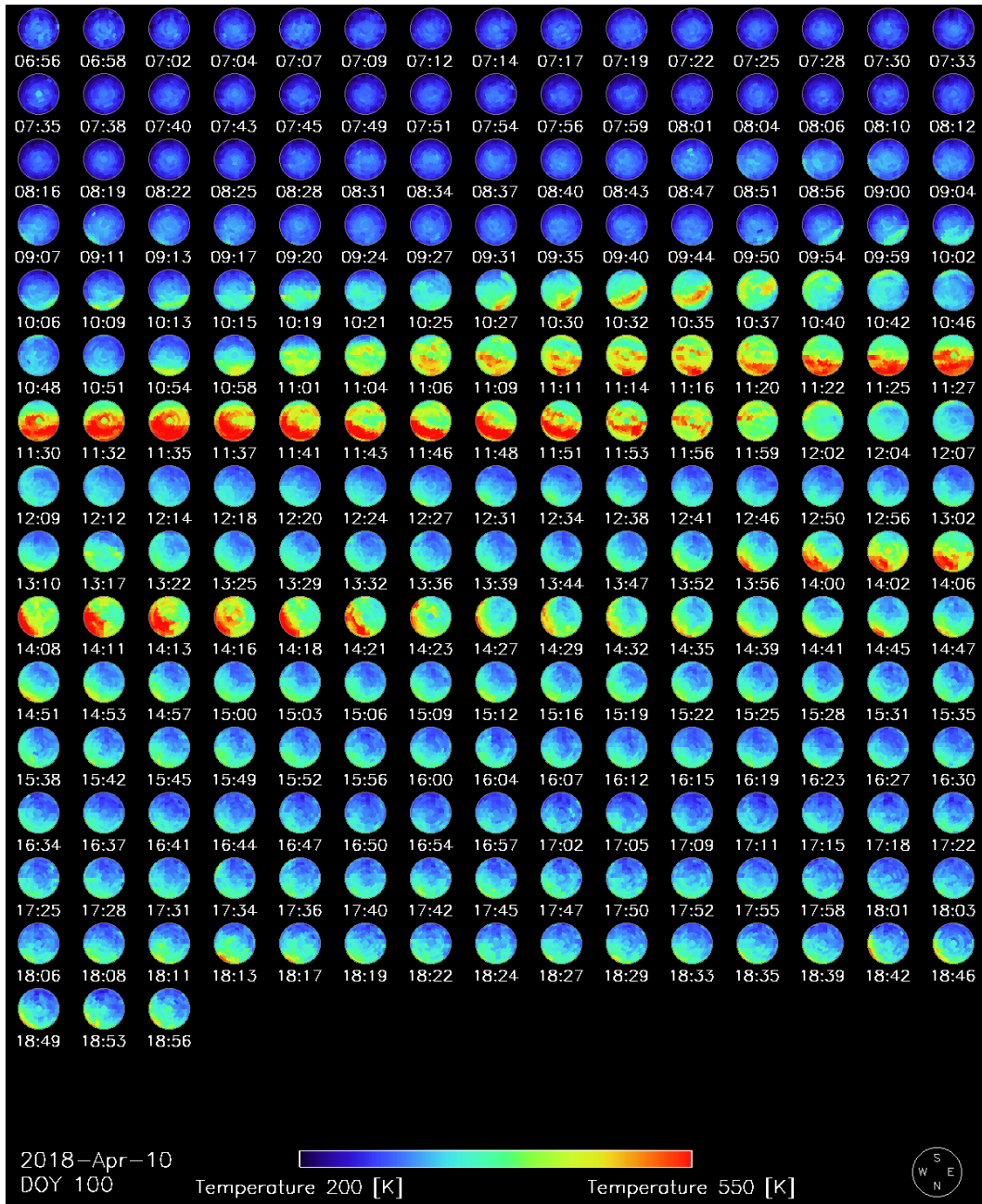


Figure 7. Skymaps of E-region Doppler temperature observed during the night of April 10, 2018, from McMurdo Station, Antarctica. Each circle shows the zenith-centered field of view of the SDI instrument at the specified time. The edge of each circle corresponds to the horizon (~ 75 degree zenith angle). Plot orientation is shown at the bottom right. The horizontal color bar at the bottom of the plot represents the temperature scale. Time in this figure is shown in the units of hours and minutes of the day in UT.

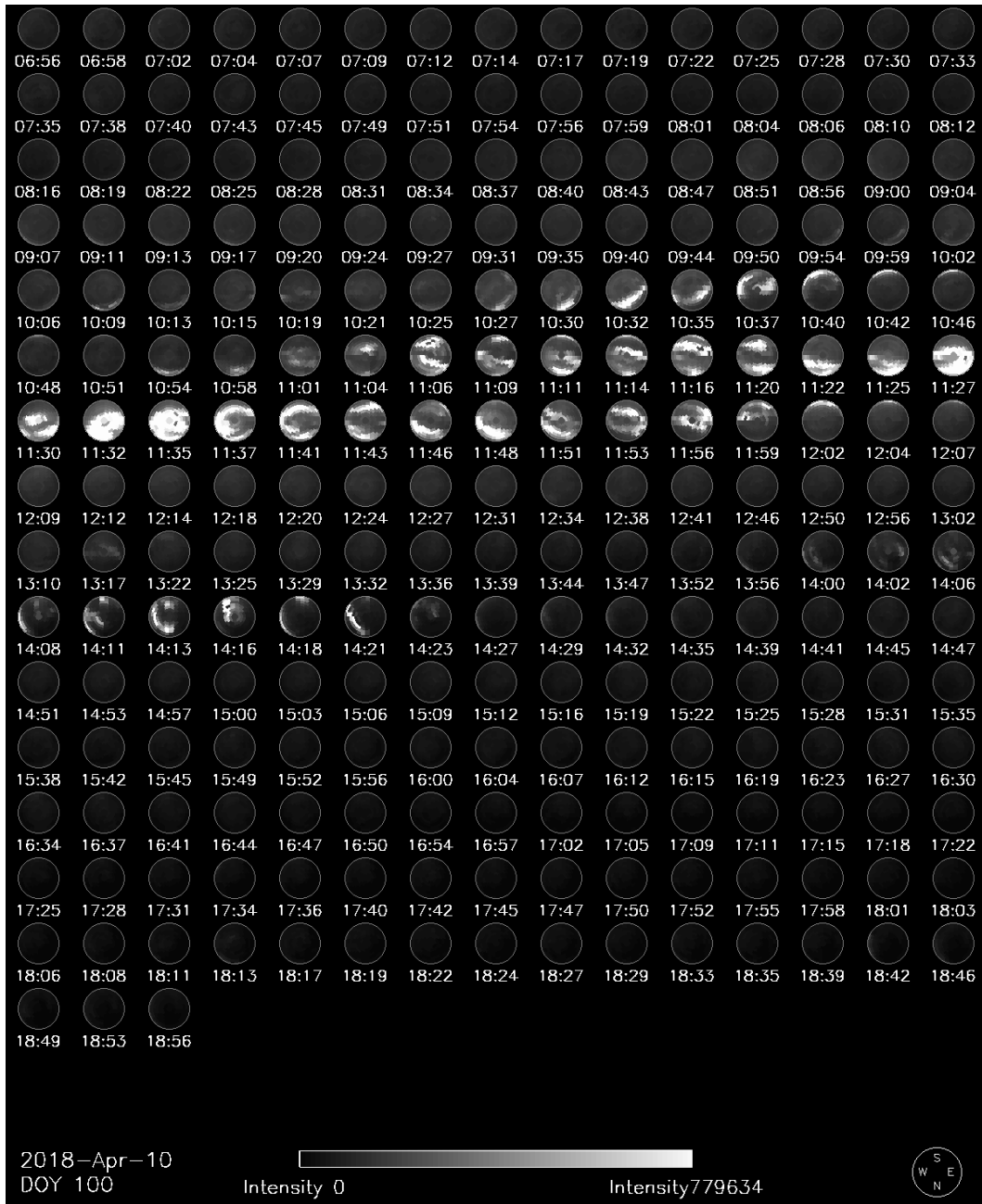


Figure 8. Same as Figure 7 but now showing skymaps of E-region airglow/auroral emission brightness displayed in arbitrary units for the night of April 10, 2018, as observed from McMurdo Station. The horizontal monochrome bar at the bottom of the plot indicates the mapping between relative brightness and gray levels.

417 *3.1.5 Concurrent Wavelike Oscillations in Temperatures and LOS Winds*

418 In addition to extracting thermospheric wind oscillations from the SDI spectra, wave-
 419 like perturbations in temperature have also been obtained. Figure 9 shows wind and tem-
 420 perature data recorded from Gakona on March 01, 2013. The wind panel shows that wave
 421 activity was relatively quiet early in the night. By contrast, large-amplitude waves pre-
 422 vailed later on this night. The middle panel shows that these wind perturbations were
 423 accompanied by temperature oscillations whose amplitude behavior over time during the
 424 night mimicked that of the winds. Qualitative inspection of Figure 9 suggests that there
 425 were several occasions with small-amplitude short-period wind fluctuations, especially
 426 between 8 UT and 9 UT. This analysis finds a typical lower cut-off period of ~ 60 min-
 427 utes for red-line LOS wind oscillations on most days. By contrast, spectral analysis of
 428 data from Gakona, Alaska on this day (not shown here for this particular day) indicated
 429 that wind oscillations occurred with statistically significant power for periods as short
 430 as ~ 30 minutes. Some of the perturbations were time-synchronous across the whole field
 431 of view; these were probably not propagating waves. On other occasions, phase progres-
 432 sions were discernible among the perturbations along different look directions. (For ex-
 433 ample phase progressions were apparent in both the wind and the temperature oscilla-
 434 tions between 14 UT and 15 UT.) It is apparent from qualitative inspection of the top
 435 panel that short-period wind oscillations were typically smaller in amplitude than long-
 436 period oscillations. Throughout the entire data set examined, magnitudes of observed
 437 oscillation amplitudes relative to experimental uncertainties were typically smaller for
 438 temperatures than they were for winds. One consequence of this is that there were fewer
 439 instances within the entire data set of unambiguous detection of wavelike activity in tem-
 440 perature, regardless of period. This difference is most extreme for shorter-period waves,
 441 for which oscillations were not typically detected in temperature, again presumably be-
 442 cause the amplitude of any short-period perturbations would not be large enough to be
 443 discernible against background noise. At times when temperature oscillations were de-
 444 tected, their amplitudes did not increase significantly from the zenith to the horizon. This
 445 is unlike the behavior observed for wind oscillations. This lack of dependence on the zenith
 446 angle for the temperature oscillation amplitudes is as expected for a scalar quantity.

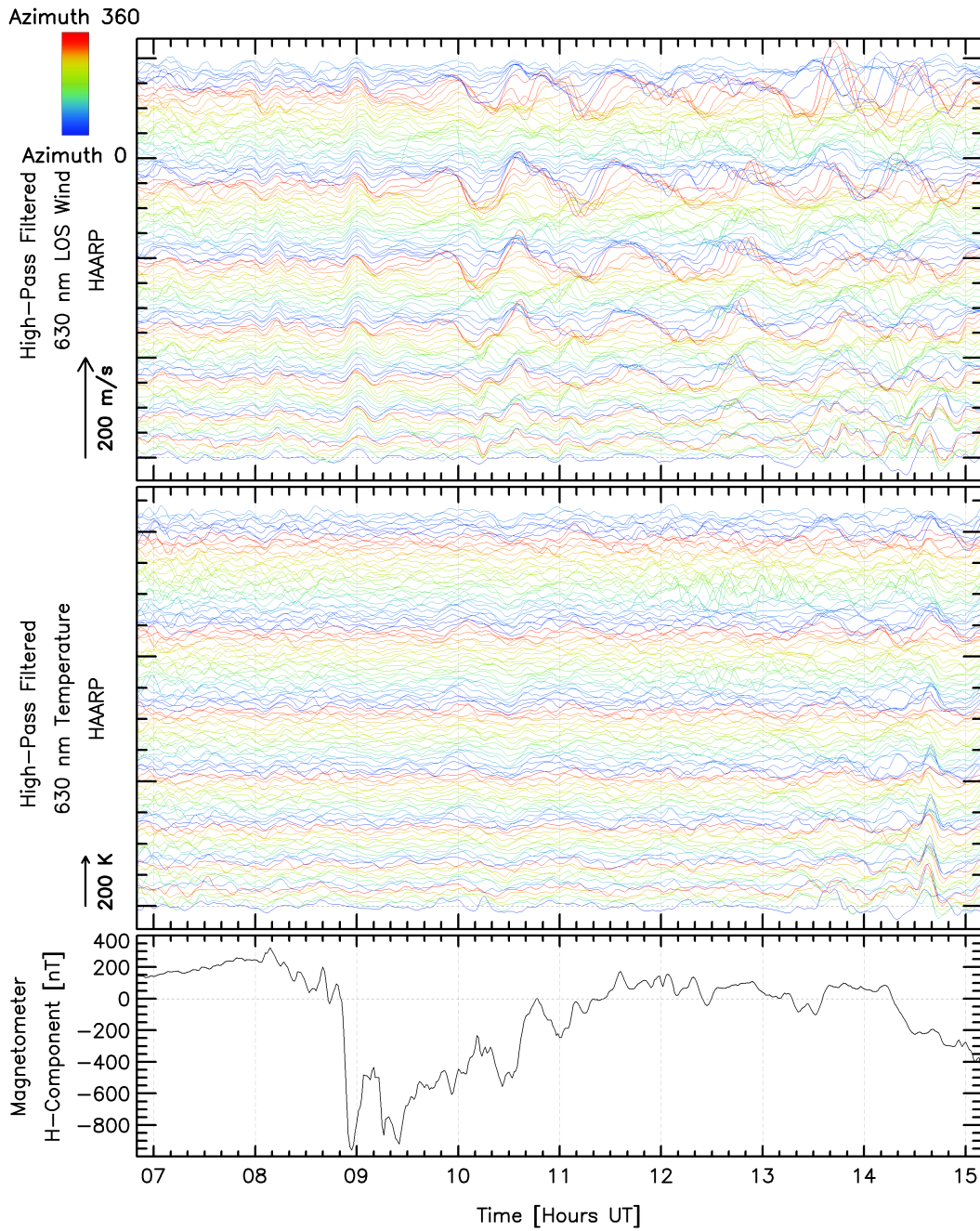


Figure 9. Same as Figure 2 but the top and middle panels respectively are showing wind and temperature oscillations recorded from Gakona, Alaska during the night of March 01, 2013. Arrows at the bottom left of the upper two panels indicate the scales of wind and temperature oscillations. The bottom panel shows the geomagnetic activity recorded at College, Alaska. On this day, the F10.7 index was 110.6 sfu, and three hourly Kp indices during (6-15) UT were 5-, 5, and 4+.

447 Figure 10 shows simultaneous perturbations in temperatures and LOS winds dur-
448 ing the night of November 7, 2017, observed from Poker Flat, Alaska. Signatures of time-
449 synchronous events, appearing as simultaneous responses occurring across almost the whole
450 all-sky field of view, are evident on several occasions. For example, the large amplitude
451 perturbations seen in both temperature and wind at ~ 10 UT are not signatures of prop-
452 agating waves. By contrast, propagating waves would be characterized by phase progres-
453 sions among the oscillations recorded along different look directions. Numerous instances
454 of such phase progressions are noticeable in the LOS wind oscillations shown in Figure
455 10. An increase in the amplitude of wind oscillations toward the horizon, as seen in Fig-
456 ure 10 is consistent with the expectation that the perturbations were associated mostly
457 with the horizontal wind. Note that, on this particular day, the all-sky field of view of
458 the SDI at Poker Flat was divided into a total of 261 zones, resulting in 261 traces for
459 wind, and similarly for temperature. (By contrast, the regular observing mode only di-
460 vides the all-sky field of view into 115 zones.) There was a high correlation between the
461 overall wave activity throughout this night with the geomagnetic activity shown in the
462 bottom panel. Similar wave activity was observed at Toolik, Alaska as well on this night
463 (not shown here).

464 By having both temperature and LOS wind perturbations, in principle, the grav-
465 ity wave polarization relations could be used to infer additional characteristics of the un-
466 derlying waves. However, the implementation of this analysis is not straightforward, be-
467 cause only the LOS component of the wind oscillations has been measured.

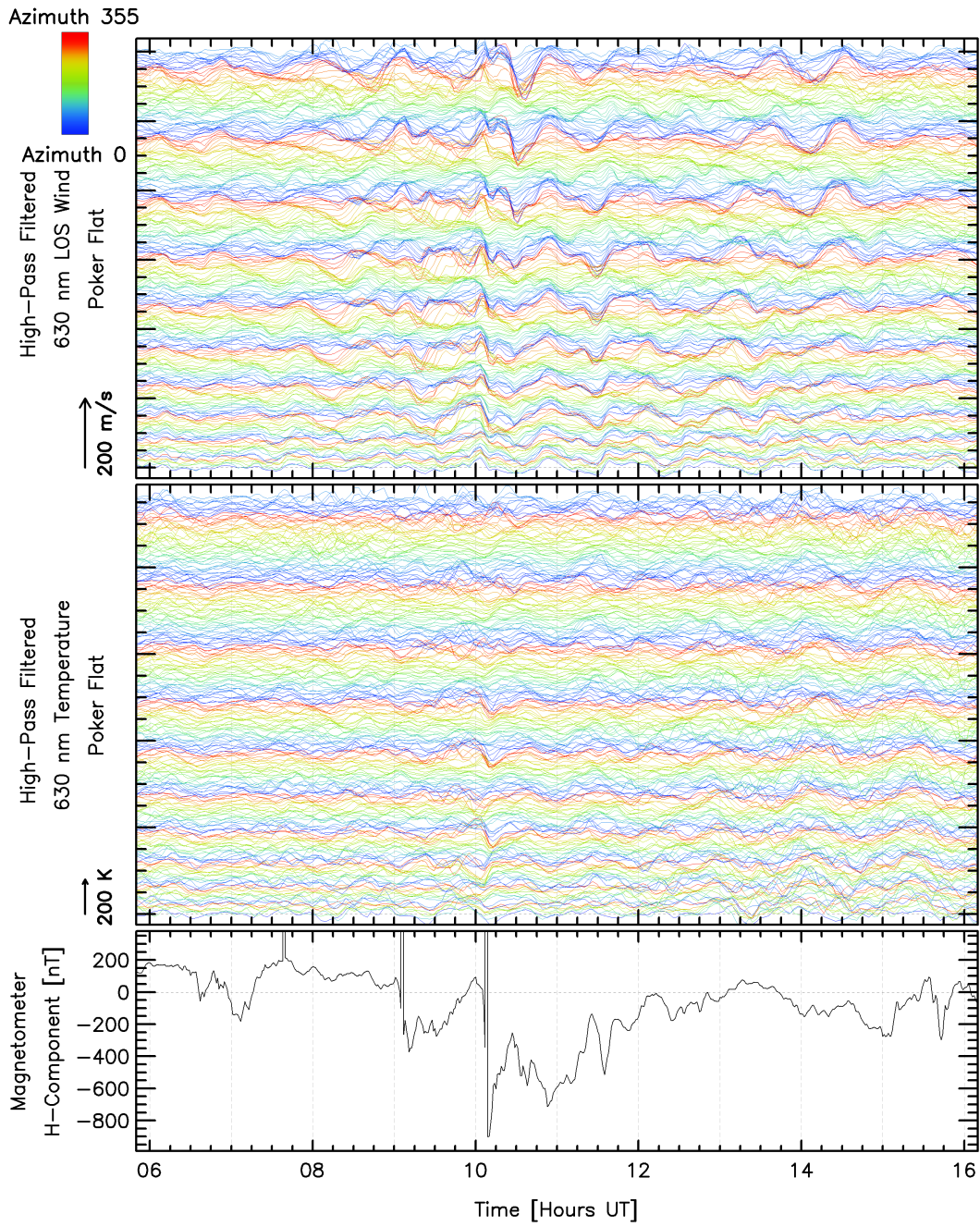


Figure 10. Same as Figure 9, but in this case showing wind and temperature oscillations as observed from Poker Flat, Alaska during the night of November 7, 2017, along with the corresponding magnetometer H-component recorded at College, Alaska. The F10.7 on this day was 67.0 sfu, and the three hourly Kp indices during (6-16) UT were 3+, 5-, 4-, and 4-.

468 3.2 Sliding Window Spectral Decomposition

469 As noted above, several previous studies have presented typical ranges of param-
470 eters for thermospheric gravity waves. In this section, estimates of temporal periods are
471 derived from the current data to determine whether the oscillations observed here are
472 consistent with previous observations. In the subsequent discussion, we will also consider
473 the consistency of the horizontal wavelength, horizontal phase speeds, and relative am-
474plitudes of the wind and temperature perturbations.

475 During any given night, it is to be expected that the observed wave period would
476 vary from zone to zone and over time. Therefore, a procedure was needed that could be
477 applied independently to a given zone and could resolve how the wave periods varied dur-
478 ing the night. To resolve time variations, subsets of the time series for a given zone were
479 taken using a sliding window of 180 minutes duration. The sliding window was initially
480 centered at the time of the first measurement that occurred more than one-half of the
481 window time after the start of observations and included all points within one-half of the
482 window time from the center. A power spectrum of the data within the window was then
483 calculated using the Lomb-Scargle technique (Lomb, 1976; Scargle, 1982). After each power
484 spectrum calculation, the time series point chosen to define the window's center time was
485 advanced by one. The final result was a set of power spectral density profiles calculated
486 as a function of the central times of the sampling windows.

487 However, the resulting power spectral measurements were distributed non-uniformly
488 in time. SDI instruments self-adjust their exposure time depending on the brightness of
489 the optical airglow/auroral emission. Since the brightness changes over time, the cor-
490 responding temperature and LOS wind observations are not uniformly spaced in time,
491 which is why the Lomb-Scargle approach was used rather than the more common fast
492 Fourier transform method.

493 Example results are shown for a selected day. To render these data as a false-color
494 2-D image, the power spectra were thus interpolated onto a regular time grid. Overall,
495 this allowed us to plot, for any selected zone, the power spectral density as a function
496 of wave period and universal time during the night. This result is referred to as a "dy-
497 namic spectrum."

498 Note that the all-sky field of view is typically divided into 115 different zones. For
 499 a given night, a separate dynamic spectrum can be produced for each of those zones, or,
 500 alternatively, an all-sky dynamic spectrum can be generated by averaging the power spec-
 501 tra from each zone. In the discussion below, one example is presented of the dynamic
 502 spectrum computed from a single zone over one night, for both red-line and green-line
 503 observations. The corresponding all-sky averaged dynamic spectra for both (red-line and
 504 green-line) observations on the same night are also presented. It is important to real-
 505 ize that the all-sky plots were produced by averaging the power spectra, rather than com-
 506 puting a single power spectrum from the LOS wind time series averaged over all zones.
 507 Because the wind component used here is aligned with the instrumental line-of-sight, av-
 508 eraging this component over the whole sky would be undesirable, as this would typically
 509 suppress most of the geophysical information present in the original measurements.

510 *3.2.1 Spectral Decomposition of E-region LOS Wind Oscillations*

511 Figures 11 and 12 show examples of dynamic spectra for the night of April 10, 2018,
 512 corresponding to E-region winds as observed from McMurdo Station, Antarctica. In these
 513 figures, x-axes represent universal time in hours while the y-axes represent wave peri-
 514 ods in minutes. The fill colors are related to the power spectral density in arbitrary units,
 515 as indicated by the color bar on the right. The black horizontal indicator line in the color
 516 bar represents the level above which the estimated power spectral density is greater than
 517 the noise, to a statistical confidence of 95%.

518 Figure 11 represents a single zone (zone number 100), centered approximately at
 519 geographic longitude: 165.53° and geographic latitude: -75.72° . This particular zone
 520 was chosen because the range of periods containing significant power varied considerably
 521 during the observations in this zone. Several spectral features appeared in this zone dur-
 522 ing the observations on this day. By contrast, there were other zones where the band of
 523 significant power remained relatively constant over time. The location of the selected zone
 524 within the all-sky field of view is shown at the bottom right by red highlighting in a small
 525 zone map. In this zone, wave periods during the observation ranged from ~ 30 minutes
 526 to as long as more than ~ 220 minutes. Oscillations with periods centered around 85 min-
 527 utes prevailed for more than 5 hours during the night. The duration of 5 hours is more
 528 than three times the 85 minutes wave period.

529 Figure 12 shows the dynamic spectrum averaged over all the 115 zones for E-region
530 winds observed on the same night and from the same location as in Figure 11. This all-
531 sky dynamic spectrum is rather simply structured, with just one significant wind oscil-
532 lation, corresponding to periods ranging from ~ 100 minutes to ~ 220 minutes. Shorter-
533 period oscillations, such as those observed in zone 100 (Figure 11), did not appear in the
534 all-sky dynamic spectrum. These short-period oscillations were examined across all the
535 zones during the night and it was found that those oscillations were present only in about
536 twenty zones that were away from the zenith in the western portion of the field of view.
537 Further, shorter-period oscillations were observed to have smaller amplitudes than longer-
538 period oscillations. Subsequently, such weaker oscillations were washed out as a result
539 of averaging the dynamic spectra across all the zones. The fact that a cluster of waves
540 with a band of periods prevailed only in a small number of zones (i.e., ~ 20) strongly sug-
541 gests that the corresponding oscillations were not instrumental artifacts. The optical con-
542 figuration of the SDI instruments is such that signal originating from every viewing zone
543 illuminates the entire aperture of the etalon. This means that any artifacts resulting from
544 unstable etalon behavior would affect all zones. There is no mechanism by which etalon
545 instability could only impact a small subset of zones. This means that oscillations seen
546 in a small subset of zones are unlikely to be of instrumental origin.

547 On this night, the majority of the power was centered among oscillations with pe-
548 riods in the range spanning ~ 120 - 160 minutes. The long-period cutoff appeared less sharp
549 relative to that for the shorter-period oscillations. However, this is most likely a conse-
550 quence of the longest periods shown in Figure 11 becoming comparable to the width of
551 the sliding time window, which has the effect of reducing the spectral resolution achiev-
552 able for the longest periods shown. Longer-period oscillations, centered around 150 min-
553 utes, detected in zone 100 were visible in the all-sky dynamic spectrum shown in Fig-
554 ure 12 as well.

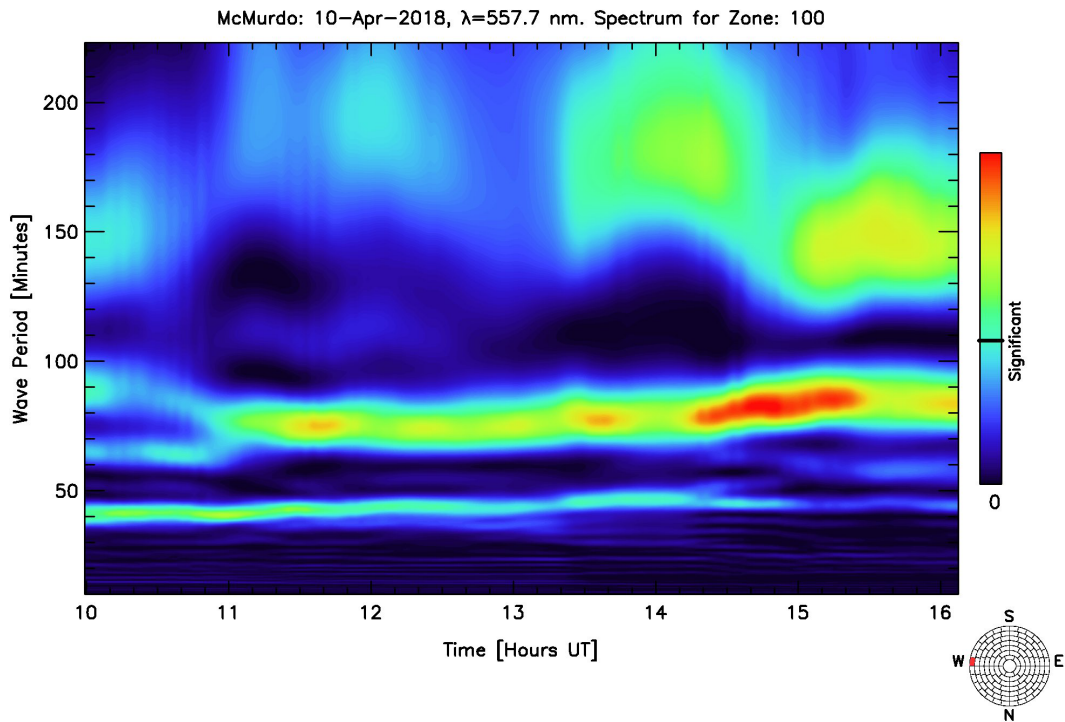


Figure 11. Dynamic Spectrum corresponding to zone number 100 for E-region winds during the night of April 10, 2018, as observed from McMurdo Station, Antarctica. Power spectral density (in arbitrary units) is represented using blue through red hues, as indicated by the color scale bar at the right. The horizontal black line on the color bar indicates the level above which there is less than 5 % probability that power calculated by the Lomb-Scargle analysis was derived solely from random noise. The small zone map at the bottom right indicates (in red highlighting) the zone chosen for the spectral decomposition.

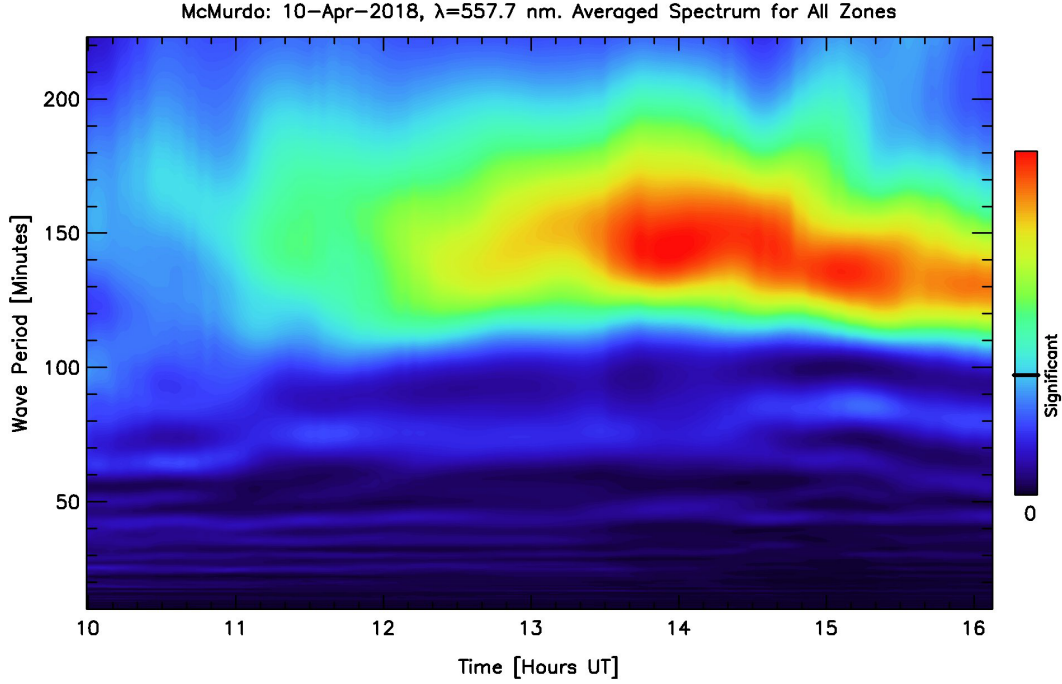


Figure 12. Green-line periodogram for the same day as Figure 11, but averaged over the whole field of view. In this case, the power spectral densities were calculated for each zone during the night and then averaged.

555

3.2.2 Spectral Decomposition of F-region LOS Wind Oscillations

556

557

558

559

560

561

562

563

564

565

566

567

568

569

Figures 13 and 14 show dynamic spectra for F-region winds as observed from McMurdo Station, Antarctica during the same night (i.e., April 10, 2018) as the green-line winds presented earlier. Figure 13 represents the dynamic spectrum derived from just one zone, zone number 52, centered approximately at geographic longitude: 165.04° and geographic latitude: -75.57° . This zone at F-region altitude corresponds to a similar geographic location as zone 100 for E-region observation shown earlier. For this zone, wave periods carrying significant power ranged over the whole night from ~ 60 minutes to more than 220 minutes. However, most of the time, the wave periods of the statistically meaningful oscillations were more confined, spanning only the approximate range from 90 to 210 minutes. Although wave amplitudes at periods shorter than those mentioned above for each altitude region were detected at times, such occasional occurrences are likely due to the high-end tail of the noise distribution, given that the indicated confidence level is rarely substantially greater than the chosen threshold of 95 %. The most significant power was observed shortly after 12 UT for periods centered around 90 minutes and af-

570 ter ~ 13 UT for periods centered around 180 minutes. As was the case of the E-region
 571 wind oscillations shown previously, the Lomb-Scargle analysis yielded lower spectral res-
 572 olution for longer periods (again as expected). Oscillations with periods less than ~ 60
 573 minutes at F-region altitudes were rarely detected in the SDI data. This is understood
 574 to be the consequence of the mechanisms for the generation and dissipation of waves in
 575 the F-region. These estimates lie within the range previously reported (e.g., Miyoshi et
 576 al., 2018). However, spectral analysis of the time series of LOS winds derived from 558
 577 nm emission (which originates at lower E-region heights) did commonly identify shorter-
 578 period (as short as ~ 30 minutes) oscillations (e.g., Figure 11).

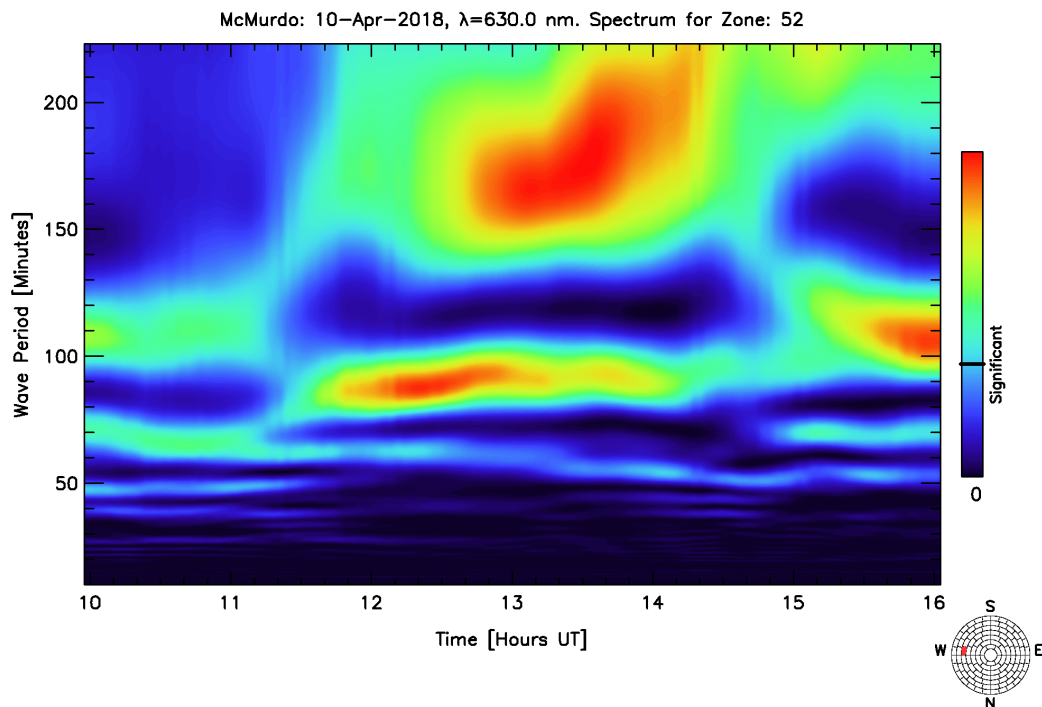


Figure 13. Same as Figure 11 but corresponding to F-region winds as observed from McMurdo Station, Antarctica on April 10, 2018, in zone number 52. The zone map at the bottom right shows, in red highlighting, the zone chosen for this dynamic spectrum plot.

579 Figure 14 shows the dynamic spectrum for F-region winds averaged over the whole
 580 field of view of the SDI instrument located at the McMurdo Station during the night of
 581 April 10, 2018. As in the previous case of E-region winds, some of the weak oscillations
 582 seen in a single zone were washed out as a result of averaging the dynamic spectra over

583 the whole sky. The band of red and green colors apparent in this plot reflects the large-
 584 scale picture of the wave activity during the night. The lowest significant period detected
 585 in the all-sky F-region LOS wind periodogram on this day was ~ 60 minutes. As before,
 586 the long-period boundary of the band of statistically significant power for F-region wind
 587 oscillations was not as sharp as the short-period boundary, again presumably as a con-
 588 sequence of limited spectral resolution for long periods. Periods where the power spec-
 589 tral density was prominent in zone 52 (Figure 13) were largely conspicuous in the all-
 590 sky dynamic spectrum as well, indicating that these oscillations were present in most zones.

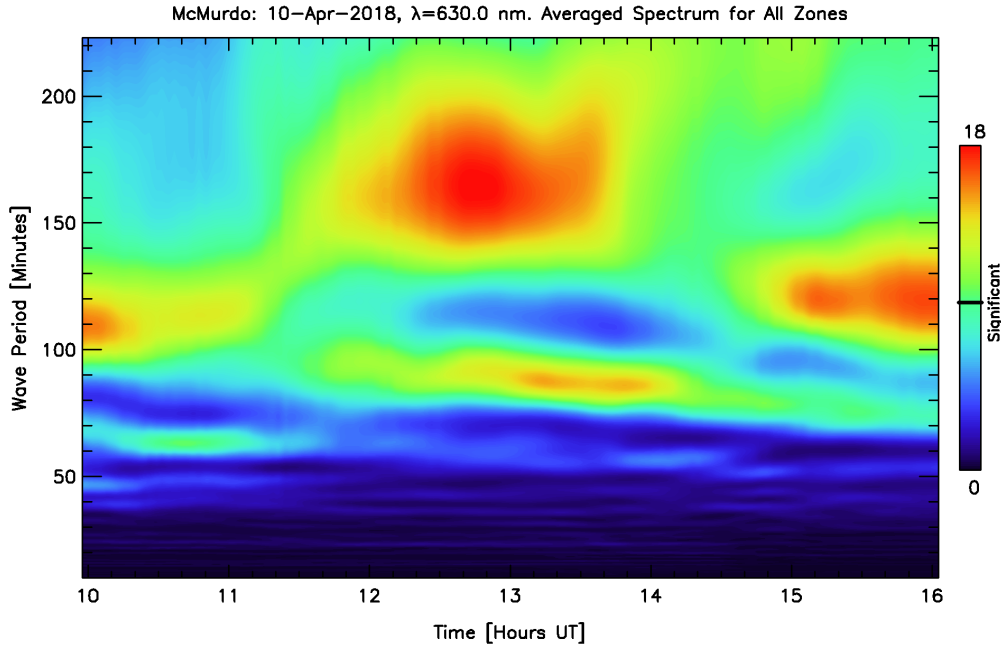


Figure 14. Same as Figure 12 but for F-region wind oscillations.

591 Note that the dynamic spectra showed substantial variability in wave periods from
 592 zone to zone. Wave periods that were statistically significant in a specific viewing zone
 593 were not necessarily significant in the all-sky dynamic spectrum.

594 In principle, these instruments could introduce oscillatory artifacts, for example,
 595 due to oscillations in etalon control parameters such as temperature. However, as dis-
 596 cussed previously, any such instrumental oscillations would almost certainly affect all zones
 597 similarly. The fact that unique oscillations were seen only in a subset of the zones strongly

598 suggests that these spectra were not instrumental artifacts. On some nights, the Lomb-
 599 Scargle analysis of data from some zones showed no periods with statistically significant
 600 wave power. Such instances were rare but did occur for some days that are included in
 601 this study.

602 4 Discussion

603 4.1 Artifacts due to E-region Emission Height Variation

604 Substantial oscillations in LOS wind at F-region altitudes were detected frequently.
 605 By contrast, the SDI data contained fewer instances of clear wavelike oscillations in ei-
 606 ther F-region temperature or E-region LOS winds. Even though the 558 nm Doppler shift
 607 and Doppler width are accurately determined by the instrument with a high signal-to-
 608 noise ratio, interpretation of these quantities is complicated by the changing height of
 609 the green-line emission layer. In the case of deriving temperatures from Doppler widths,
 610 the vertical temperature gradient is so strong in the E-region that the dominant pertur-
 611 bations in high pass filtered 558 nm temperature time series arise simply because of the
 612 emission height variations due to changing characteristic energy of the auroral precip-
 613 itation that excites the emission. Thus, although oscillations were seen in E-region tem-
 614 peratures, we presume that these mostly would have been due to changes in the aurora
 615 rather than the actual fluctuations in the background temperature at a constant height.
 616 In the case of 558 nm LOS wind measurements, the vertical gradients of horizontal wind
 617 in the E-region can also be strong (Larsen, 2002; Branning et al., 2022), which means
 618 that height variations of the emission layer may add artifacts to the high pass filtered
 619 LOS wind time series that could, at times, dominate over other signals, such as those
 620 that might indicate the presence of atmospheric waves. Periods when such artifacts ap-
 621 pear can be easily identified as “bursts” of noise in the wind time series correlated with
 622 periods when the 558 nm Doppler temperature is changing rapidly. An example of such
 623 behavior is shown in Figure 15. In this figure, the fitted zonal wind is noisy and vari-
 624 able when the fitted temperature is more variable. Note that much of the variability in-
 625 dicated by the wind error bars arises not because the fitted winds have large uncertainty
 626 but because the fitted wind field is non-uniform. Temperature variations indicate changes
 627 in the emission height - and that could mean the measured winds would change if there
 628 was a strong vertical gradient in the wind field. In this experiment, there is no way to
 629 determine whether strong vertical gradients were present - but the figure at least shows

630 that some of the wind variability could be associated with height changes. Such changes,
 631 if they do occur, would contribute to perturbations in the wave plots. However, an ex-
 632 amination of roughly 20 years of 558 nm SDI data shows that the strength of this con-
 633 tribution can be quite variable. Overall, it is thus not surprising that E-region wind os-
 634 cillations look noisier in the SDI data than those generally observed for F-region winds.

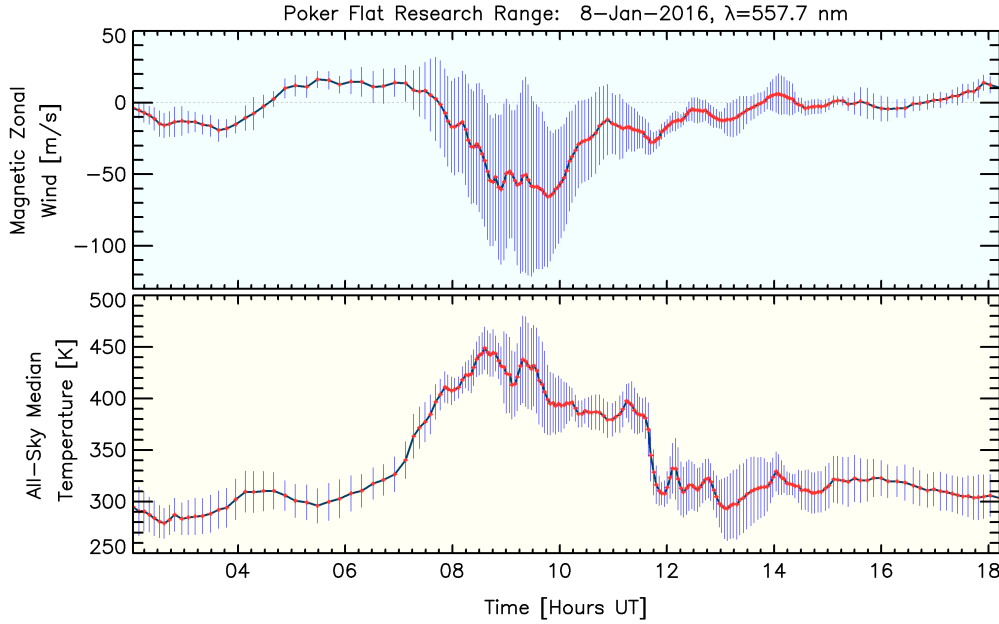


Figure 15. Fitted temperatures and winds derived from 558 nm spectra for Jan 8, 2016, at Poker Flat. The top and bottom panels respectively show the fitted zonal wind speeds and all-sky median temperatures as a function of time. In both panels, the “error bars” show the standard deviation of the corresponding 115 values of the fitted quantity at each observing time. Thus, the error bars are not solely indicating statistical uncertainty in the measurements – in many cases, longer error bars arise because of true geophysical variability across the field of view (however, statistical uncertainty will always have some contribution.)

635 4.2 Qualitative Testing of the Plausibility of Wave Interpretation

636 SDI instruments have multiple viewing zones that project to an extended geographic
 637 region in the thermosphere. For waves propagating across the instrument’s field of view,
 638 systematic delays are expected between the times at which a given phase front would
 639 cross viewing zones that are separated with respect to each other along the direction of

640 wave propagation. There should thus be systematic phase differences between pertur-
 641 bations observed by the individual zones, with the particular pattern of phase differences
 642 being characteristic of the speed and direction of the wave's phase propagation. Further,
 643 the observed LOS wind oscillation is typically modulated in part by the viewing azimuth.
 644 This is because the contribution to the observed wave perturbation is modulated by the
 645 dot product of the viewing azimuth direction and the direction of horizontal motion as-
 646 sociated with the wave. Note that no such viewing azimuth dependence applies to the
 647 LOS component of vertical wave oscillations. Rather, this contribution is instead mod-
 648 ulated by the cosine of the observing zenith angle.

649 If wind perturbations occurring in the atmosphere were only in the horizontal com-
 650 ponents, the amplitude of the LOS component of this oscillation would be zero when look-
 651 ing in the zenith and, for other look directions, it would increase in proportion to the
 652 sine of the zenith angle. In most instances, this general behavior was observed for the
 653 LOS wind, although the amplitude of the oscillation in the zenith zone was almost never
 654 seen to drop entirely to zero. Usually, small but non-zero oscillation amplitudes were ob-
 655 served in the zenith zone, with the amplitude of these oscillations increasing with zenith
 656 angles (as expected) out to a maximum near the horizon. These characteristics indicate
 657 that the wind perturbations had both horizontal and vertical components associated with
 658 them, with the horizontal component typically being larger. The observed systematic
 659 dependence of LOS wind perturbation amplitude on the zenith angle would be extremely
 660 unlikely to arise purely because of instrumental artifacts. Instead, observed perturba-
 661 tions are almost certainly of geophysical origin. Temperature oscillations are, by con-
 662 trast, scalar quantities that would not manifest any amplitude dependence on zenith or
 663 azimuth angle – which was largely consistent with the actual behavior observed. Nev-
 664 ertheless, a small level of zenith angle dependence was seen in the temperature oscilla-
 665 tions as well. The exact reason for this weak effect is unknown, although one possibil-
 666 ity involves the changing volume of the atmosphere enclosed by the intersection of the
 667 airglow layer with the solid angle viewed by each zone.

668 Moreover, for a uniform field of monochromatic plane phase fronts, and a given zenith
 669 angle, there would be a pair of diametrically opposite azimuths for which the LOS com-
 670 ponents of the horizontal wind oscillation amplitudes would maximize, and they would
 671 be zero when viewing perpendicular to those azimuths. However, as depicted in Figure
 672 16 (and in most other cases inspected), such simple and systematic azimuthal variation

673 of perturbation amplitudes were not observed. It is inferred from this that the actual
 674 wind perturbations in the SDI data were usually not due to a uniform field of monochro-
 675 matic waves in the horizontal wind. Rather, the actual wave fields in the thermosphere
 676 must always be more complicated indicating, for any given time, the presence of a range
 677 of periods and multiple propagation directions within the field of view. Nevertheless, Fig-
 678 ure 16 clearly shows that the wind oscillation phase does vary with azimuth, as expected
 679 for a geophysical field of propagating waves.

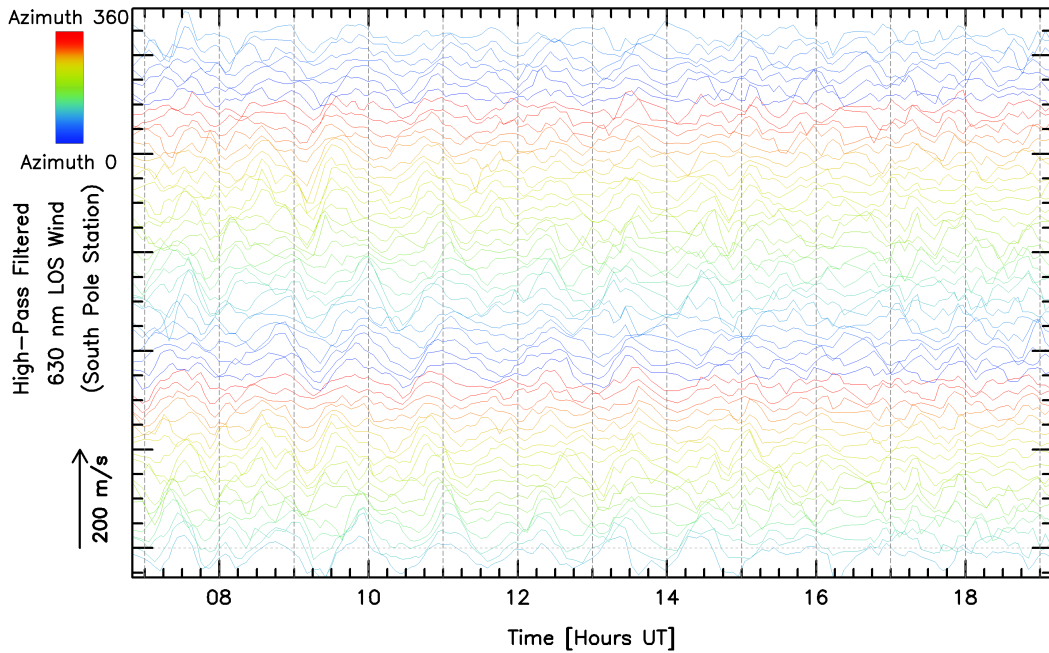


Figure 16. High-pass filtered LOS wind perturbations for selected zones spanning the two outermost rings of the SDI field of view (zones 63 to 114) on April 10, 2018, as observed from the South Pole Station (same day as in the middle panel of Figure 2). The reason for selecting just two rings is to allow phase relationships between successive zones to be more readily discernible.

680 As expected, instances of relative phase differences between oscillations in differ-
 681 ent zones were frequently seen. However, there were other times when no phase differ-
 682 ences between oscillations were seen regardless of the look azimuths and look elevations.
 683 These events were characterized by large amplitude fluctuations occurring almost time-
 684 synchronously across much of the field of view. Such attributes arise in the SDI data as
 685 shown, for example, in the top two panels of Figure 3 at $\sim 8:30$ UT and in the 558 nm
 686 wind panel of Figure 6 at ~ 11 UT. These time-synchronous responses cannot be signa-

687 tures of propagating waves. Rather, two possible ways in which such signatures could
688 arise in the SDI data can be postulated.

689 Firstly, impulsive changes in magnetospheric forcing can impact a wide geographic
690 area of the thermosphere simultaneously. These signatures could thus indicate directly-
691 driven atmospheric perturbations responding simultaneously over a wide geographic area
692 to sudden changes in magnetospheric forcing. The result would be a time-synchronous
693 response across most if not all of the SDI instrument's field of view. It is noted, how-
694 ever, that even if the wind changes time-synchronously, amplitude and phase shifts in
695 the observed LOS wind components are still expected due to the projection angle with
696 varying viewing azimuth. (No such azimuth dependency is expected for temperature per-
697 turbations.)

698 A second (and perhaps more significant) issue arises because sudden changes in au-
699 roral precipitation can cause this remote sensing technique to introduce artifacts in the
700 measured winds and temperatures. For example, the time variation of emission bright-
701 ness can distort recorded spectra because of the way the etalon scans over time, partic-
702 ularly for zones near the zenith. More importantly, as described previously, the altitude
703 of the observed emission can change in response to changing characteristic energy of au-
704 roral precipitation. If the observed quantity (wind or temperature) varies with height
705 in the background atmosphere, then the change in characteristic energy will cause changes
706 in the measurements that do not reflect any actual temporal change in the real atmo-
707 sphere (Sica et al., 1986; McCormac et al., 1987).

708 Time-synchronous events typically occurred superposed upon a preexisting ambi-
709 ent wave field. Nevertheless, the time-synchronous events almost always were observed
710 during times of substantial impulsive auroral and geomagnetic forcing of the atmosphere.
711 This forcing often excited significant oscillations that were resolvable for several hours
712 after the initial event. Thus, even though the time-synchronous perturbations do not ap-
713 pear to themselves be signatures of wave perturbations, they usually indicated the on-
714 set of forcing events that did produce subsequently observable waves.

715 Time-synchronous perturbations can be identified readily in the SDI data but may
716 not be as conspicuous to an instrument with observations in only a few look directions.
717 Observations based on a single or small number of look directions would be unable to
718 distinguish between traveling waves and time-synchronous non-wavelike oscillations, due

719 to the inability to track phase shifts among the different look directions. This could lead
 720 every oscillation to be interpreted as a signature of a traveling wave. However, as explained
 721 above, this current study has shown that there are many instances when such an assump-
 722 tion would be likely to be incorrect, at least for large perturbations observed in auro-
 723 ral latitudes. We, therefore, caution that inferences regarding wave activity that are based
 724 on Doppler spectral observations incorporating only a small number of look directions
 725 (or possibly only one) might be biased by artifacts associated with the types of time-synchronous
 726 responses that have been identified here.

727 As discussed in earlier sections, waves in the thermosphere do not exclusively origi-
 728 nate in situ. Some portion of the wave spectrum is caused by driving that occurs in the
 729 lower atmosphere, with perturbations subsequently propagating up to the thermosphere,
 730 albeit possibly after one or more instances of breaking and exciting secondary waves (Smith
 731 et al., 2013; Vadas et al., 2018). During this process of wave breaking and critical layer
 732 filtering, the original shorter-period waves typically fail to reach thermospheric heights.
 733 Further, the dissipation of waves as a result of rapid diffusion suppresses short-period
 734 waves in the F-region (Fritts & Alexander, 2003). Based on these considerations, the re-
 735 sulting F-region wind oscillations would be expected to be smoother (with less power at
 736 high frequencies) than the corresponding E-region oscillations. The observations were
 737 indeed consistent with this expectation.

738 4.3 Quantitative Consistency Tests

739 As noted, it is difficult to know the extent to which the oscillations observed here
 740 are due to atmospheric gravity waves, versus other geophysical processes or (possibly)
 741 instrumental mechanisms. However, one potential “back-of-the-envelope” diagnostic is
 742 to test whether relations between observed perturbations in the horizontal wind, verti-
 743 cal wind, and temperature are at least not inconsistent with theoretical expectations for
 744 thermospheric gravity waves. Application of simplified gravity wave polarization rela-
 745 tions for a harmonic oscillation (e.g., Hines, 1960) predicts the following relationships
 746 between the various wave perturbation amplitudes and wave parameters

$$\frac{u'}{\omega k_x k_z C^2} = \frac{z'}{-\omega k_x^2 C^2} = \frac{\rho'/\bar{\rho}}{i(\gamma - 1) g k_x^2}, \quad (1)$$

747 where u' and z' are the amplitudes of the wave's horizontal and vertical oscillations
 748 respectively, $\rho'/\bar{\rho}$ is the fractional mass density perturbation amplitude, ω is the intrinsic
 749 (angular) frequency of the wave oscillation, k_x and k_z are the horizontal and vertical
 750 wave numbers, g is the acceleration due to Earth's gravity, γ is the adiabatic constant
 751 (with a value of 5/3 for a monatomic gas), and $C = \sqrt{\gamma g H}$ is the speed of phase
 752 propagation for sound waves with H being the scale height. Also, i is $\sqrt{-1}$, which merely
 753 indicates that the density oscillations are 90° out of phase with the wind oscillations.

754 Assuming the relative temperature perturbation amplitude T'/\bar{T} is the same as the
 755 relative density amplitude, and writing the Brunt-Väisälä frequency as

$$\omega_b \simeq \sqrt{\frac{\gamma - 1}{\gamma} \frac{g}{H}}, \quad (2)$$

756 Equations (1) can be rearranged to give

$$\frac{T'}{\bar{T}} \simeq \frac{\omega_b^2}{g\omega} z', \quad (3)$$

$$\text{and } \frac{k_x}{k_z} = \frac{z'}{u'}, \quad (4)$$

757 The quantities u' , z' , T' , \bar{T} , and ω obviously vary considerably among the data ex-
 758 amples presented here. For each of these parameters, the largest observed perturbation
 759 amplitudes in this study were a factor of ~ 5 times as large as the smallest observed per-
 760 turbation amplitude. Nevertheless, by examining many days of data, we find that it is
 761 possible to meaningfully estimate a “typical” observed amplitude, at least to the preci-
 762 sion needed to test whether the results are consistent with gravity wave theory. Result-
 763 ing estimates for these quantities in the 630 nm (F-region) data were $u' \simeq 50 \text{ m s}^{-1}$,
 764 $z' \simeq 20 \text{ m s}^{-1}$, $T'/\bar{T} \simeq 6\%$ (*i.e.*, 50 K/800 K), and $\omega \simeq 2\pi/(3600 \text{ s})$. (Here, z' was es-
 765 timated from the LOS wind oscillation amplitude in the zenith zone, whereas u' was de-
 766 termined from the amplitudes in the outer zones.)

767 Inserting the observed estimates for u' and z' into Equation 4 shows that $k_z \simeq 2.5k_x$
 768 for the waves observed here. This can then be substituted into the usual non-dissipative
 769 dispersion relation for thermospheric gravity waves (e.g., Vadas & Fritts, 2005)

$$\omega = \sqrt{\frac{k_x^2 \omega_b^2}{k_z^2 + k_x^2 + \left(\frac{1}{2H}\right)^2}} \quad (5)$$

770 and solved for k_x , from which the horizontal wavelength of these waves (with temporal
771 period $\simeq 60$ minutes) can be estimated to be

$$\lambda_x \simeq 2\pi\sqrt{29}H \simeq 1520 \text{ km}, \quad (6)$$

772 which was obtained using estimates of $\omega_b \simeq 2\pi/(12 \text{ minutes})$ and $H \simeq 45 \text{ km}$ –
773 which are representative for conditions at F-region heights. The characteristic horizon-
774 tal intrinsic phase speeds for the observed waves can then be estimated as

$$v_{px} = \frac{\omega}{k_x} = \frac{2\pi/3600 \text{ s}}{2\pi/1520 \text{ km}} \simeq 420 \text{ m s}^{-1}. \quad (7)$$

775 These horizontal wavelengths and horizontal phase speeds are well within the ranges
776 previously observed for these parameters of thermospheric gravity waves at F-region heights
777 (e.g. Miyoshi et al., 2018; England et al., 2020).

778 Also, for a Brunt-Väisällä period of 12 minutes, and using the representative val-
779 ues encountered in this study of $\omega \sim 2\pi/(60 \text{ minutes})$ and $z' \sim 20 \text{ m/s}$, the right-hand
780 side of Equation 3 predicts that the relative temperature perturbations due to the ob-
781 served waves would be around 9%. As calculated previously, the observed relative tem-
782 perature perturbation is $\sim 6\%$. Here, the predicted T' is a little larger than the observed
783 T' . Although these values are slightly different, several of the contributing factors for
784 T' have large relative uncertainties – i.e., 100% or more. Given the uncertainty in the
785 input values, the calculated T'/\bar{T} is not inconsistent with observations.

786 Finally, the predicted 90° phase shift between wind and temperature oscillations
787 should provide a demanding test of whether the data are consistent with waves. Unfor-
788 tunately, the observed waveforms were seldom monochromatic enough for this to be a
789 definitive test. In Figure 17, a small portion of the data was zoomed-in so that the phase
790 relationship can be examined readily by making individual traces apparent. As shown
791 by Figure 17, there was seldom, if ever, a simple phase relation between observed wind
792 and temperature oscillations. In particular, wind oscillations with a period of ~ 60 min-
793 utes are easily discernible toward the top of the upper panel of Figure 17. However, the
794 corresponding temperature oscillations are more difficult to discern.

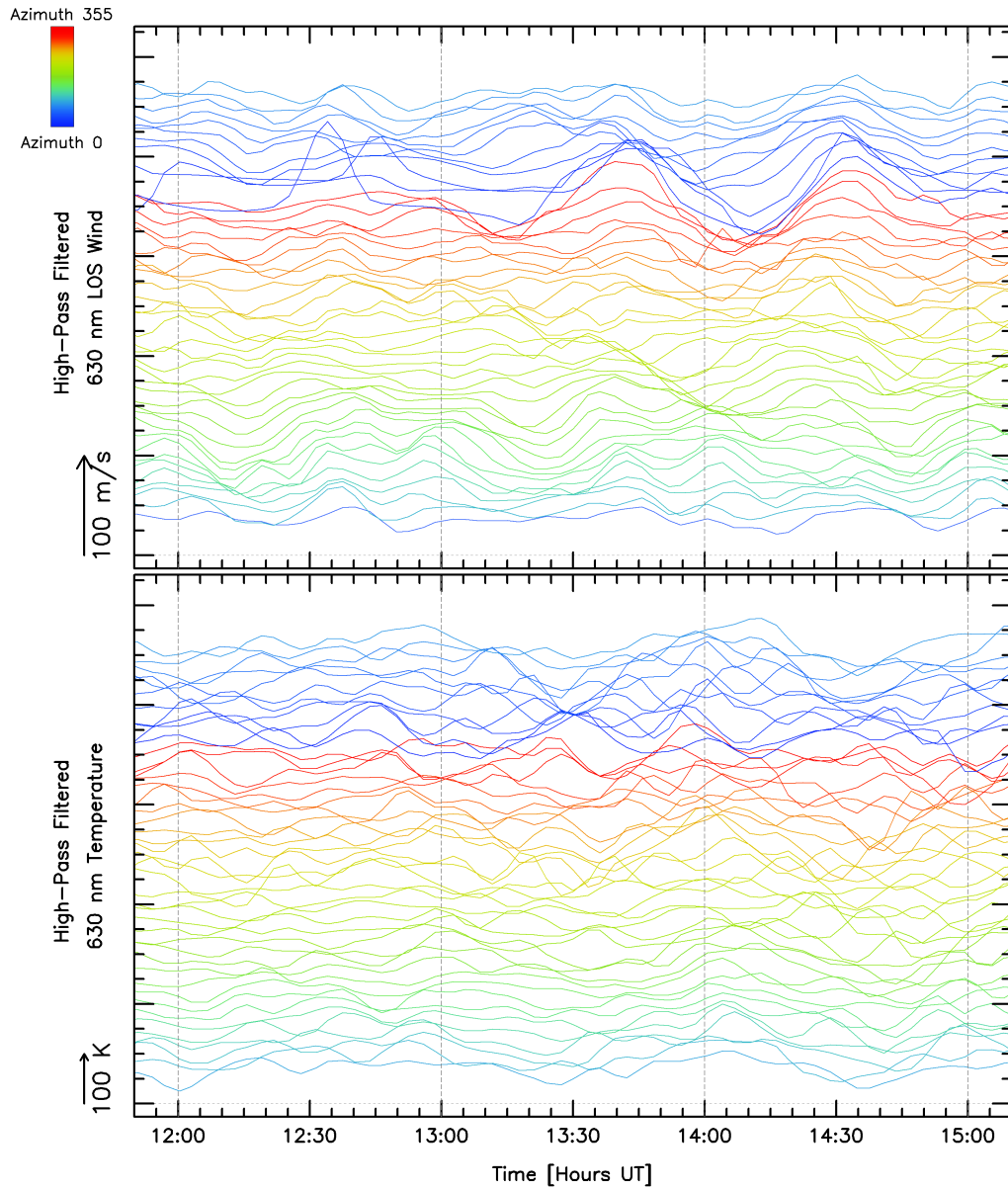


Figure 17. Zoomed-in subset of temperature and LOS wind oscillations observed on Nov 7, 2017, from Poker Flat, Alaska. This figure only shows three hours of data for selected zones (zones 218-261) in the outermost ring of the SDI field of view. These oscillations were generally complicated, such that it is difficult to discern any systematic phase relationship between wind and temperature oscillations.

795 It seems likely that the perturbations observed here are signatures of important pro-
 796 cesses in the thermospheric energy and momentum budgets. It is, therefore, crucial to

797 understand the extent to which these perturbations are representative of traveling waves
798 propagating in the real thermosphere. The next step would be to use the SDI data to
799 investigate the distributions of phase speeds, horizontal wavelength, vertical wavelength,
800 propagation directions, intrinsic periods, etc. Robust reconstruction of phase fronts would
801 be facilitated by the multiple observing stations and look directions provided by the SDI
802 instrument array. It would then be possible to infer the various wave parameters. How-
803 ever, this analysis would require fitting a two-dimensional field of traveling phase fronts
804 to the data, which itself is a non-trivial forward modeling problem even if there is just
805 one simple monochromatic plane wave field present. If there are multiple wave packets,
806 each with their own individual amplitudes, phase, propagation direction, period, etc.,
807 the analysis would become far more difficult.

808 As a final note, this study required manual inspection of hundreds of days of data
809 from each site. Statistical metrics have not yet been developed to rigorously quantify the
810 occurrence frequency of discernible wave activity. However, qualitatively, it was noticed
811 that truly quiescent conditions were uncommon in the F-region above most of the SDI
812 sites. For all but one site, it was unusual to encounter a day when the instrument was
813 functioning well, and the sky was clear, but the F-region wave signal was indistinguish-
814 able from noise. The one exception to this was the site at Mawson, for which the impres-
815 sion was formed that quiescent days were more common. To test this, approximately 130
816 clear nights of high-pass filtered 630 nm LOS wind data were examined. These obser-
817 vations were acquired from Mawson in 2011. We were unable to confidently recognize
818 wave perturbations on roughly 40% of these days. By contrast, the unambiguous absence
819 of waves was rare for all other sites. These results suggest that the wave field above Maw-
820 son can relax to a more quiescent state than it can elsewhere. One possible interpreta-
821 tion is that there is a background contribution of waves propagating up from the lower
822 atmosphere that is seen by most sites apart from Mawson. This perhaps indicates that
823 the orographic and/or meteorological generation of lower atmospheric waves is less sig-
824 nificant at this site.

825 5 Conclusions

826 This study examined oscillatory perturbations in measurements of thermospheric
827 temperature and wind derived from optical Doppler spectra. Significant oscillatory per-
828 turbations were unambiguously detected using high-pass temporal filtering. Their char-

acteristics suggest that they are of geophysical origin. The objective of studying them was to examine the hypothesis that these perturbations could be signatures of gravity wave activity. Perturbation amplitudes were observed to increase considerably during increased geophysical activity. While F-region wind perturbations were almost always detected at some level, the SDI instruments were less able to resolve oscillations in F-region temperatures or E-region winds. This is understood as arising because the perturbation amplitudes of F-region temperature and E-region winds are smaller relative to other sources of measurement variability and errors for these quantities. Nevertheless, the data do contain instances of apparent wavelike perturbations in those quantities as well.

The dependence of the perturbation amplitudes on geophysical activity, viewing zenith angle, and viewing azimuth angle all indicate that the observed fluctuations were of geophysical origin rather than being due to measurement artifacts. Phase relations between the time series for the various viewing zones suggest that the observed perturbations were often consistent with expectations for a (typically complicated) field of traveling waves, although this was not always the case. Many instances of time-synchronous perturbations across all viewing zones were observed, that cannot be interpreted as signatures of waves.

Nevertheless, the data suggest that the technique can detect thermospheric gravity waves and, further, it shows that wave activity is common in Earth's thermosphere at auroral latitudes. Additionally, the data suggest that the wave response to the geomagnetic activity is similar in either hemisphere.

Azimuthal variation of phases throughout all of the data suggests that the wave field in the Earth's thermosphere is seldom a simple set of monochromatic plane phase fronts. Rather, it appears that the wave field is more typically composed of many different wave packets with widely varying amplitudes, phases, and propagation directions. Presumably, if such wave fields could be visualized, they would appear reminiscent of the complicated field of surface waves often seen on the ocean.

Sliding-window Lomb-Scargle analysis was performed on the LOS wind time series from selected nights to analyze how the spectrum of observed wave periods varied as a function of time during the night. The resulting periodograms showed that the wave spectra varied from zone to zone. Further, spectra also varied within individual zones

861 over the course of a night. The shortest observed periods for F-region wind oscillations
862 with statistically significant power were typically 60 minutes. By contrast, the spectrum
863 of E-region waves extended to shorter periods – i.e., as short as 30 minutes. Oscillations
864 with periods up to 220 minutes were detected both at E- and F-region altitudes. Longer-
865 period oscillations may occur, but those cannot be resolved with the current technique.
866 Thermospheric gravity waves have been observed in previous studies over a broad range
867 of periods extending from a few tens of minutes up to more than 12 hours (Richmond,
868 1978; Vadas & Fritts, 2006; Ford et al., 2008; Klausner et al., 2009; Katamzi-Joseph et
869 al., 2019). The wave periods observed here fall well within this range. Observed E-region
870 wind oscillations were often noisier and less monochromatic than the corresponding F-
871 region wind perturbations, resulting in broader Lomb-Scargle spectra for E-region data.
872 As discussed in section 3.1.4, geophysical noise due to the altitude variation of the 558
873 nm emission layer could have contributed to this spectral broadening of the E-region time
874 series. By contrast, the F-region LOS wind oscillations were relatively smooth, as ex-
875 pected.

876 The initial expectation was that oscillations observed during quiet geomagnetic con-
877 ditions could be indications of disturbances propagating up from below, because in-situ
878 wave generation would, presumably, be weak. Although wave perturbations likely do prop-
879 agate up from the lower atmosphere, this study did not resolve such a component, be-
880 cause of the nearly ubiquitous background activity. More detailed analysis will be re-
881 quired to determine the relative contributions of in-situ forcing versus upward propaga-
882 tion.

883 There is more information in the SDI data than has been examined in this current
884 work. Future studies will focus on phase lags and relative amplitudes of oscillations be-
885 tween time series recorded in different zones. Although relatively rare, it is expected that
886 there would be some instances when the wave field is sufficiently simple that the rela-
887 tive amplitudes and phases between the zones could be used to infer the properties of
888 at least the dominant perturbations that are present. Measuring these phase lags would
889 characterize properties such as the period, phase speed, and direction of phase propa-
890 gation. This analysis would not be possible for observations made in a single look direc-
891 tion and would be less robust if only a small number of directions were viewed.

892 Acknowledgments

893 This research was supported by NSF award numbers 1341545 and 1452333. Magnetome-
 894 ter observations used in this work were provided by Geosciences Australia (Mawson),
 895 the New Zealand Antarctic Program (Scott Base), and the US Geological Survey (Col-
 896 lege), and accessed via the archive maintained by the International INTERMAGNET
 897 program (www.intermagnet.org). We also thank INTERMAGNET for promoting high
 898 standards of magnetic observatory practice. Scanning Doppler Imager data are available
 899 at http://sdi_server.gi.alaska.edu/sdi_web_plots. Solar radio flux density (F10.7)
 900 data were adopted from [https://www.spaceweather.gc.ca/forecast-prevision/solar](https://www.spaceweather.gc.ca/forecast-prevision/solar-solaire/solarflux/sx-5-flux-en.php)
 901 [-solaire/solarflux/sx-5-flux-en.php](https://www.spaceweather.gc.ca/forecast-prevision/solar-solaire/solarflux/sx-5-flux-en.php).

902 References

- 903 Anderson, C., Conde, M., & McHarg, M. (2012a). Neutral thermospheric dynamics
 904 observed with two scanning doppler imagers: 1. monostatic and bistatic winds.
 905 *Journal of Geophysical Research: Space Physics*, *117*(A3).
- 906 Anderson, C., Conde, M., & McHarg, M. (2012b). Neutral thermospheric dynamics
 907 observed with two scanning doppler imagers: 3. horizontal wind gradients. *Journal*
 908 *of Geophysical Research: Space Physics*, *117*(A5).
- 909 Branning, K., Conde, M., Larsen, M., & Troyer, R. (2022). Resolving vertical
 910 variations of horizontal neutral winds in earth’s high latitude space-atmosphere
 911 interaction region (sair). *Journal of Geophysical Research: Space Physics*, *127*(5),
 912 e2021JA029805.
- 913 Bruinsma, S. L., & Forbes, J. M. (2008). Medium-to large-scale density variability as
 914 observed by champ. *Space Weather*, *6*(8).
- 915 Conde, M., Bristow, W., Hampton, D., & Elliott, J. (2018). Multiinstrument stud-
 916 ies of thermospheric weather above alaska. *Journal of Geophysical Research: Space*
 917 *Physics*, *123*(11), 9836–9861.
- 918 Conde, M., Craven, J., Immel, T., Hoch, E., Stenbaek-Nielsen, H., Hallinan, T., ...
 919 others (2001). Assimilated observations of thermospheric winds, the aurora, and
 920 ionospheric currents over alaska. *Journal of Geophysical Research: Space Physics*,
 921 *106*(A6), 10493–10508.
- 922 Conde, M., & Smith, R. (1998). Spatial structure in the thermospheric horizontal
 923 wind above poker flat, alaska, during solar minimum. *Journal of Geophysical Re-*

- 924 *search: Space Physics, 103(A5), 9449–9471.*
- 925 Djuth, F., Sulzer, M., Elder, J., & Wickwar, V. (1997). High-resolution studies
926 of atmosphere-ionosphere coupling at arecibo observatory, puerto rico. *Radio Sci-*
927 *ence, 32(6), 2321–2344.*
- 928 Djuth, F., Sulzer, M., Gonzales, S., Mathews, J., Elder, J., & Walterscheid, R.
929 (2004). A continuum of gravity waves in the arecibo thermosphere? *Geophysical*
930 *Research Letters, 31(16).*
- 931 England, S. L., Greer, K. R., Solomon, S. C., Eastes, R. W., McClintock, W. E., &
932 Burns, A. G. (2020). Observation of thermospheric gravity waves in the southern
933 hemisphere with gold. *Journal of Geophysical Research: Space Physics, 125(4),*
934 *e2019JA027405.*
- 935 Ford, E., Aruliah, A., Griffin, E., & McWhirter, I. (2008). Statistical analysis of
936 thermospheric gravity waves from fabry-perot interferometer measurements of
937 atomic oxygen. In *Annales geophysicae* (Vol. 26, pp. 29–45).
- 938 Fritts, D. C., & Alexander, M. J. (2003). Gravity wave dynamics and effects in the
939 middle atmosphere. *Reviews of geophysics, 41(1).*
- 940 Fukushima, D., Shiokawa, K., Otsuka, Y., & Ogawa, T. (2012). Observation of
941 equatorial nighttime medium-scale traveling ionospheric disturbances in 630-nm
942 airglow images over 7 years. *Journal of Geophysical Research: Space Physics,*
943 *117(A10).*
- 944 Gabrielse, C., Nishimura, T., Chen, M., Hecht, J. H., Kaeppler, S. R., Gillies, D. M.,
945 . . . Evans, J. S. (2021). Estimating precipitating energy flux, average energy, and
946 hall auroral conductance from themis all-sky-imagers with focus on mesoscales.
947 *Frontiers in Physics, 9, 744298.*
- 948 Galvan, D. A., Komjathy, A., Hickey, M. P., & Mannucci, A. J. (2011). The 2009
949 samoa and 2010 chile tsunamis as observed in the ionosphere using gps total elec-
950 tron content. *Journal of Geophysical Research: Space Physics, 116(A6).*
- 951 Garcia, R. F., Bruinsma, S., Massarweh, L., & Doornbos, E. (2016). Medium-scale
952 gravity wave activity in the thermosphere inferred from goce data. *Journal of*
953 *Geophysical Research: Space Physics, 121(8), 8089–8102.*
- 954 Hays, P., Nagy, A. F., & Roble, R. (1969). Interferometric measurements of the 6300
955 a doppler temperature during a magnetic storm. *Journal of Geophysical Research,*
956 *74(16), 4162–4168.*

- 957 Hecht, J., Strickland, D., & Conde, M. (2006). The application of ground-based
 958 optical techniques for inferring electron energy deposition and composition change
 959 during auroral precipitation events. *Journal of atmospheric and solar-terrestrial*
 960 *physics*, *68*(13), 1502–1519.
- 961 Hernandez, G. (1982). Vertical motions of the neutral thermosphere at midlatitude.
 962 *Geophysical Research Letters*, *9*(5), 555–557.
- 963 Hickey, M., Schubert, G., & Walterscheid, R. (2010). Atmospheric airglow fluctu-
 964 ations due to a tsunami-driven gravity wave disturbance. *Journal of Geophysical*
 965 *Research: Space Physics*, *115*(A6).
- 966 Hines, C. O. (1960). Internal atmospheric gravity waves at ionospheric heights.
 967 *Canadian Journal of Physics*, *38*(11), 1441–1481.
- 968 Hocke, K., Schlegel, K., et al. (1996). A review of atmospheric gravity waves and
 969 travelling ionospheric disturbances: 1982–1995. In *Annales geophysicae* (Vol. 14,
 970 p. 917).
- 971 Innis, J. (2000). Deceleration of the high-latitude thermospheric wind by polar cap
 972 gravity waves. *Geophysical research letters*, *27*(23), 3813–3816.
- 973 Innis, J., Greet, P., & Dyson, P. (1996). Fabry-perot spectrometer observations of
 974 the auroral oval/polar cap boundary above mawson, antarctica. *Journal of Atmo-*
 975 *spheric and Terrestrial Physics*, *58*(16), 1973–1988.
- 976 Itani, R., & Conde, M. (2021). Characterizing unexpectedly localized slowing of the
 977 thermospheric cross-polar jet of neutral wind over alaska in the midnight sector.
 978 *Journal of Geophysical Research: Space Physics*, *126*(10), e2020JA028916.
- 979 Johnson, F., Hanson, W., Hodges, R., Coley, W., Carignan, G., & Spencer, N.
 980 (1995). Gravity waves near 300 km over the polar caps. *Journal of Geophysi-*
 981 *cal Research: Space Physics*, *100*(A12), 23993–24002.
- 982 Kaeppler, S., Hampton, D., Nicolls, M., Strømme, A., Solomon, S., Hecht, J., &
 983 Conde, M. (2015). An investigation comparing ground-based techniques that
 984 quantify auroral electron flux and conductance. *Journal of Geophysical Research:*
 985 *Space Physics*, *120*(10), 9038–9056.
- 986 Katamzi-Joseph, Z. T., Aruliah, A. L., Oksavik, K., Habarulema, J. B., Kauristie,
 987 K., & Kosch, M. J. (2019). Multi-instrument observations of large-scale atmo-
 988 spheric gravity waves/traveling ionospheric disturbances associated with enhanced
 989 auroral activity over svalbard. *Advances in Space Research*, *63*(1), 270–281.

- 990 Killeen, T., Craven, J., Frank, L., Ponthieu, J.-J., Spencer, N., Heelis, R., . . . Carig-
 991 nan, G. (1988). On the relationship between dynamics of the polar thermosphere
 992 and morphology of the aurora: Global-scale observations from dynamics explorers
 993 1 and 2. *Journal of Geophysical Research: Space Physics*, *93*(A4), 2675–2692.
- 994 Killeen, T., & Roble, R. (1988). Thermosphere dynamics: Contributions from the
 995 first 5 years of the dynamics explorer program. *Reviews of Geophysics*, *26*(2),
 996 329–367.
- 997 Klausner, V., Fagundes, P., Sahai, Y., Wrasse, C., Pillat, V., & Becker-Guedes, F.
 998 (2009). Observations of gw/tid oscillations in the f2 layer at low latitude during
 999 high and low solar activity, geomagnetic quiet and disturbed periods. *Journal of*
 1000 *Geophysical Research: Space Physics*, *114*(A2).
- 1001 Larsen, M. (2002). Winds and shears in the mesosphere and lower thermosphere:
 1002 Results from four decades of chemical release wind measurements. *Journal of Geo-*
 1003 *physical Research: Space Physics*, *107*(A8), SIA–28.
- 1004 Lomb, N. R. (1976). Least-squares frequency analysis of unequally spaced data. *As-*
 1005 *trophysics and space science*, *39*(2), 447–462.
- 1006 McCormac, F., Killeen, T. L., Nardi, B., & Smith, R. (1987). How close are
 1007 ground-based fabry-perot thermospheric wind and temperature measurements
 1008 to exospheric values? a simulation study. *Planetary and space science*, *35*(10),
 1009 1255–1265.
- 1010 Miyoshi, Y., Jin, H., Fujiwara, H., & Shinagawa, H. (2018). Numerical study of
 1011 traveling ionospheric disturbances generated by an upward propagating gravity
 1012 wave. *Journal of Geophysical Research: Space Physics*, *123*(3), 2141–2155.
- 1013 Nicolls, M., Vadas, S., Meriwether, J., Conde, M., & Hampton, D. (2012). The
 1014 phases and amplitudes of gravity waves propagating and dissipating in the ther-
 1015 mosphere: Application to measurements over alaska. *Journal of Geophysical*
 1016 *Research: Space Physics*, *117*(A5).
- 1017 Oliver, W., Otsuka, Y., Sato, M., Takami, T., & Fukao, S. (1997). A climatology of
 1018 f region gravity wave propagation over the middle and upper atmosphere radar.
 1019 *Journal of Geophysical Research: Space Physics*, *102*(A7), 14499–14512.
- 1020 Oyama, S., Ishii, M., Murayama, Y., Shinagawa, H., Buchert, S., Fujii, R., & Kof-
 1021 man, W. (2001). Generation of atmospheric gravity waves associated with auroral
 1022 activity in the polar f region. *Journal of Geophysical Research: Space Physics*,

- 1023 106(A9), 18543–18554.
- 1024 Paulino, I., Medeiros, A., Vadas, S., Wrasse, C., Takahashi, H., Buriti, R., . . . others
1025 (2016). Periodic waves in the lower thermosphere observed by oi630 nm airglow
1026 images. In *Annales geophysicae* (Vol. 34, pp. 293–301).
- 1027 Richmond, A. (1978). Gravity wave generation, propagation, and dissipation in
1028 the thermosphere. *Journal of Geophysical Research: Space Physics*, 83(A9), 4131–
1029 4145.
- 1030 Scargle, J. D. (1982). Studies in astronomical time series analysis. ii-statistical
1031 aspects of spectral analysis of unevenly spaced data. *The Astrophysical Journal*,
1032 263, 835–853.
- 1033 Sica, R., Rees, M., Roble, R. G., Hernandez, G., & Romick, G. (1986). The alti-
1034 tude region sampled by ground-based doppler temperature measurements of the oi
1035 15867 k emission line in aurorae. *Planetary and space science*, 34(5), 483–488.
- 1036 Smith, S., Vadas, S., Baggaley, W., Hernandez, G., & Baumgardner, J. (2013).
1037 Gravity wave coupling between the mesosphere and thermosphere over new
1038 zealand. *Journal of Geophysical Research: Space Physics*, 118(5), 2694–2707.
- 1039 Vadas, S. L., & Azeem, I. (2020). Concentric secondary gravity waves in the ther-
1040 mosphere and ionosphere over the continental united states on 25-26 march
1041 2015 from deep convection. *Journal of Geophysical Research: Space Physics*,
1042 e2020JA028275.
- 1043 Vadas, S. L., & Fritts, D. C. (2005). Thermospheric responses to gravity waves: In-
1044 fluences of increasing viscosity and thermal diffusivity. *Journal of Geophysical Re-*
1045 *search: Atmospheres*, 110(D15).
- 1046 Vadas, S. L., & Fritts, D. C. (2006). Influence of solar variability on gravity wave
1047 structure and dissipation in the thermosphere from tropospheric convection. *Jour-*
1048 *nal of Geophysical Research: Space Physics*, 111(A10).
- 1049 Vadas, S. L., & Liu, H.-l. (2009). Generation of large-scale gravity waves and neutral
1050 winds in the thermosphere from the dissipation of convectively generated gravity
1051 waves. *Journal of Geophysical Research: Space Physics*, 114(A10).
- 1052 Vadas, S. L., Zhao, J., Chu, X., & Becker, E. (2018). The excitation of secondary
1053 gravity waves from local body forces: Theory and observation. *Journal of Geo-*
1054 *physical Research: Atmospheres*, 123(17), 9296–9325.
- 1055 Yeh, K. C., & Liu, C. H. (1974). Acoustic-gravity waves in the upper atmosphere.

1056 *Reviews of Geophysics*, 12(2), 193–216.

1057 Yiğit, E., & Medvedev, A. S. (2012). Gravity waves in the thermosphere during a
1058 sudden stratospheric warming. *Geophysical Research Letters*, 39(21).

1059 Yiğit, E., & Medvedev, A. S. (2019). Obscure waves in planetary atmospheres:
1060 on earth and on other planets, internal gravity waves shape the dynamics and
1061 thermodynamics of the atmosphere. *Physics today*, 72(6).

1062 Yu, Y. (2007). *Model studies of time-dependent ducting for high-frequency grav-*
1063 *ity waves and associated airglow responses in the upper atmosphere.* University of
1064 Central Florida.